2023-06

ENERGY OPTIMAL GUIDANCE OF UAS IN TIME-VARYING 3-DIMENSIONAL WIND ENVIRONMENTS

Lalumandier, Luke J.

Monterey, CA; Naval Postgraduate School

NAVAL POSTGRADUATE SCHOOL

MONTEREY, CALIFORNIA

THESIS

ENERGY OPTIMAL GUIDANCE OF UAS IN TIME-VARYING 3-DIMENSIONAL WIND ENVIRONMENTS

by

Luke J. Lalumandier

June 2023

Thesis Advisor: Vladimir N. Dobrokhodov
Co-Advisor: Mark Karpenko

THIS PAGE INTENTIONALLY LEFT BLANK

REPORT DOCUMENTATION PAGE	*Form Approved OMB No. 0704-0188*

1. AGENCY USE ONLY *(Leave blank)*	**2. REPORT DATE** June 2023	**3. REPORT TYPE AND DATES COVERED** Master's thesis

4. TITLE AND SUBTITLE ENERGY OPTIMAL GUIDANCE OF UAS IN TIME-VARYING 3-DIMENSIONAL WIND ENVIRONMENTS	**5. FUNDING NUMBERS** RMK69; RMK9R
6. AUTHOR(S) Luke J. Lalumandier	
7. PERFORMING ORGANIZATION NAME(S) AND ADDRESS(ES) Naval Postgraduate School Monterey, CA 93943-5000	**8. PERFORMING ORGANIZATION REPORT NUMBER**
9. SPONSORING / MONITORING AGENCY NAME(S) AND ADDRESS(ES) Operational Energy Office	**10. SPONSORING / MONITORING AGENCY REPORT NUMBER**

11. SUPPLEMENTARY NOTES The views expressed in this thesis are those of the author and do not reflect the official policy or position of the Department of Defense or the U.S. Government.

12a. DISTRIBUTION / AVAILABILITY STATEMENT Approved for public release. Distribution is unlimited.	**12b. DISTRIBUTION CODE** A

13. ABSTRACT (maximum 200 words)

Increasing the fuel efficiency of military aircraft provides a tactical advantage to the aircraft operator. Increases in fuel efficiency in turn increase an aircraft's time on station, allow higher payload capacity, expand operational range, and reduce operating costs. Since the performance increases from fuel-efficiency compound over time, high endurance aircraft, like intelligence, surveillance, and reconnaissance (ISR) unmanned aerial systems (UAS), are a particularly applicable class of aircraft for research. This paper presents an approach for accomplishing these fuel savings through the design of an energy-optimal trajectory planning algorithm. This is done by modeling the performance of a UAS and defining the power required to maintain flight as the cost function in three dimensions and time. The time and location-varying effects of air density and wind are included in this model. Then, using Pontryagin's Minimum Principle, the problem becomes a boundary value problem, which is then numerically solved, generating the energy-optimal trajectory. This results in an energy-optimal trajectory solution that utilizes favorable atmospheric effects like tailwinds and updrafts, and avoids detrimental atmospheric effects, like headwinds.

14. SUBJECT TERMS Optimal Guidance, ISR, UAS, UAV, Onboard Autonomy, Ultra-High Endurance Aircraft, Fuel Efficiency, Energy Efficiency, Pontryagin Maximum Principle, Optimal Control	**15. NUMBER OF PAGES** 101
	16. PRICE CODE

17. SECURITY CLASSIFICATION OF REPORT	**18. SECURITY CLASSIFICATION OF THIS PAGE**	**19. SECURITY CLASSIFICATION OF ABSTRACT**	**20. LIMITATION OF ABSTRACT**
Unclassified	Unclassified	Unclassified	UU

NSN 7540-01-280-5500

Standard Form 298 (Rev. 2-89)
Prescribed by ANSI Std. 239-18

THIS PAGE INTENTIONALLY LEFT BLANK

Approved for public release. Distribution is unlimited.

ENERGY OPTIMAL GUIDANCE OF UAS IN TIME-VARYING 3-DIMENSIONAL WIND ENVIRONMENTS

Luke J. Lalumandier
Ensign, United States Navy
BS, University of Illinois, Urbana-Champaign, 2022

Submitted in partial fulfillment of the
requirements for the degree of

MASTER OF SCIENCE IN AEROSPACE ENGINEERING

from the

NAVAL POSTGRADUATE SCHOOL
June 2023

Approved by: Vladimir N. Dobrokhodov
Advisor

Mark Karpenko
Co-Advisor

Brian S. Bingham
Chair, Department of Mechanical and Aerospace Engineering

THIS PAGE INTENTIONALLY LEFT BLANK

ABSTRACT

Increasing the fuel efficiency of military aircraft provides a tactical advantage to the aircraft operator. Increases in fuel efficiency in turn increase an aircraft's time on station, allow higher payload capacity, expand operational range, and reduce operating costs. Since the performance increases from fuel-efficiency compound over time, high endurance aircraft, like intelligence, surveillance, and reconnaissance (ISR) unmanned aerial systems (UAS), are a particularly applicable class of aircraft for research. This paper presents an approach for accomplishing these fuel savings through the design of an energy-optimal trajectory planning algorithm. This is done by modeling the performance of a UAS and defining the power required to maintain flight as the cost function in three dimensions and time. The time and location-varying effects of air density and wind are included in this model. Then, using Pontryagin's Minimum Principle, the problem becomes a boundary value problem, which is then numerically solved, generating the energy-optimal trajectory. This results in an energy-optimal trajectory solution that utilizes favorable atmospheric effects like tailwinds and updrafts, and avoids detrimental atmospheric effects, like headwinds.

THIS PAGE INTENTIONALLY LEFT BLANK

Table of Contents

List of Figures

List of Tables

THIS PAGE INTENTIONALLY LEFT BLANK

Acknowledgments

I would like to acknowledge and thank the great team of faculty in the MAE Department of Naval Postgraduate School that provided immense guidance in the development of this thesis. Their patience, suggestions, and insight substantially contributed to the completion of this thesis in the short time frame of one year. I would like to particularly thank:

Professor Isaac Michael Ross, who introduced me to the field of optimal control theory. His classes provided me with a strong foundation in optimal control theory, significantly contributing to my understanding of the subject. When numerical solutions provided unexpected behavior, he could quickly identify the potential issues, without even needing to look at the code. This is all before mentioning him as the inventor of DIDO, the numerical solver at the heart of this thesis.

Professor Vladimir Dobrokhodov, my primary advisor, whose guidance was instrumental. When I first met with him to inquire about doing a trajectory optimization thesis, he warned me that the project would not be easy. At that moment, and every moment after, he would always be very direct — something I always really appreciated. During weekly meetings, he provided me with advice at every step of the way. He continuously ensured I was aware of and meeting the timeline for completion. At times when I would go down a rabbit hole, he would provide caution while simultaneously allowing me to explore further.

Professor Mark Karpenko, my co-advisor, who spent immense time with me working through implementation errors in DIDO, reviewing the model, and discussing ways to adjust the scaling. His door was always open, and he never hesitated to sit down and discuss any questions I had. This was the case for both this thesis and the classes he co-taught with Professor Ross. He was instrumental in solidifying concepts foundational to optimal control theory.

THIS PAGE INTENTIONALLY LEFT BLANK

CHAPTER 1:
Introduction

1.1 Nomenclature

AR	Wing aspect ratio	U	Control variable
C_D	Aircraft drag coefficient	V_a	Aircraft velocity (air relative)
C_{D0}	Zero-lift aircraft drag coefficient	V_g	Aircraft velocity (inertial relative)
C_L	Aircraft lift coefficient	w_{NED}	Wind velocity (navigation frame)
e	Oswald efficiency number	W	Aircraft weight
g	Gravitational constant ($9.815\ \frac{m}{s^2}$)	X	State variable
H	Hamiltonian	x	Distance North
h	Altitude	y	Distance East
J	Cost function	α	Angle of attack
K	Drag polar constant	β	Side-slip angle
K_{p1}	Profile drag constant	η	Propulsion efficiency
K_{p2}	Induced drag constant	λ	Costate variable
m	Aircraft mass	ρ	Atmospheric density
N	Number of nodes	ψ	Heading angle
P_{req}	Power required	ϕ	Bank angle
S	Aircraft planform area	γ	Climb angle (inertial relative)
t	Time	γ_a	Climb angle (air relative)

1.2 Introduction

In the field of guidance, the most fundamental problem is determining an optimal trajectory between two points. This problem has been around since the days of ships of sail when sailors would contend with the effects of sea currents on their vessels. Neglecting the effects of wind and sea currents, a great circle route is the fastest route from the origin to a desired point. However, upon incorporating wind and sea currents, this problem becomes much more complex. In dynamic optimization, this problem would be posed by Ernst Zermelo as

what would become known as “Zermelo’s navigation problem” [1]. The optimal path was shown to be one that utilizes more favorable winds and avoids unfavorable winds without going too far out of the great circle way.

This problem can equally be posed for aircraft in modern times, as the role of naval forces has expanded from the seas to include the skies. However, instead of minimizing time like in “Zermelo’s navigation problem”, the goal of this thesis is to design a system to generate a trajectory where the total power (or other constrained resource) required to get from origin to destination is minimized. This results in a guidance solution that creates flight plans which utilize tailwinds and updrafts and avoid headwinds. To accomplish this, a model of the aircraft has been developed which utilizes atmospheric data, relevant state, and control variables. Then, using Pontryagin’s Minimum Principle, the needed conditions for transforming the problem to a boundary value problem as well as providing the conditions for optimality were designed. Finally, a numerical solution is obtained, generating the energy-optimal trajectory.

Increasing the fuel efficiency of military aircraft provides numerous performance benefits that extend far beyond reducing environmental impacts — it provides a distinct tactical advantage. This can manifest itself as increased time on station, providing enhanced situational awareness and intelligence-gathering capabilities for military operations. Also, it can allow the platform to carry a heavier payload, which in turn can allow for additional or heavier sensor packages to be added to the aircraft. Additionally, greater fuel efficiency increases the operational range of the aircraft. This allows a single airbase to have a greater area of coverage. Another effect of decreasing fuel consumption is reducing demand on supporting logistics networks and decreasing per flight hour cost of operation. The performance gains from increased fuel efficiency compound over time. This makes high-endurance aircraft, such as ISR UAS, see the largest advantage from implementing an energy-efficient trajectory planning algorithm.

1.3 Ultra-Long Endurance UAS

This thesis contributes to POTION — an Operational Energy Prototyping Fund program — which is developing software to recommend the most efficient flight plan to fleet UAS operators. New ultra-high endurance platforms now demonstrate ranges of thousands of miles

and can stay airborne for days, all without refueling. With the complexity and uncertainty of weather patterns, it is nearly impossible for human operators to create a flight plan for these aircraft that does not leave performance on the table. While this project is built to be applicable to various platforms, the Hybrid Tiger and Vanilla UAS have been directly involved in the development of this flight planning software.

1.3.1 Hybrid Tiger

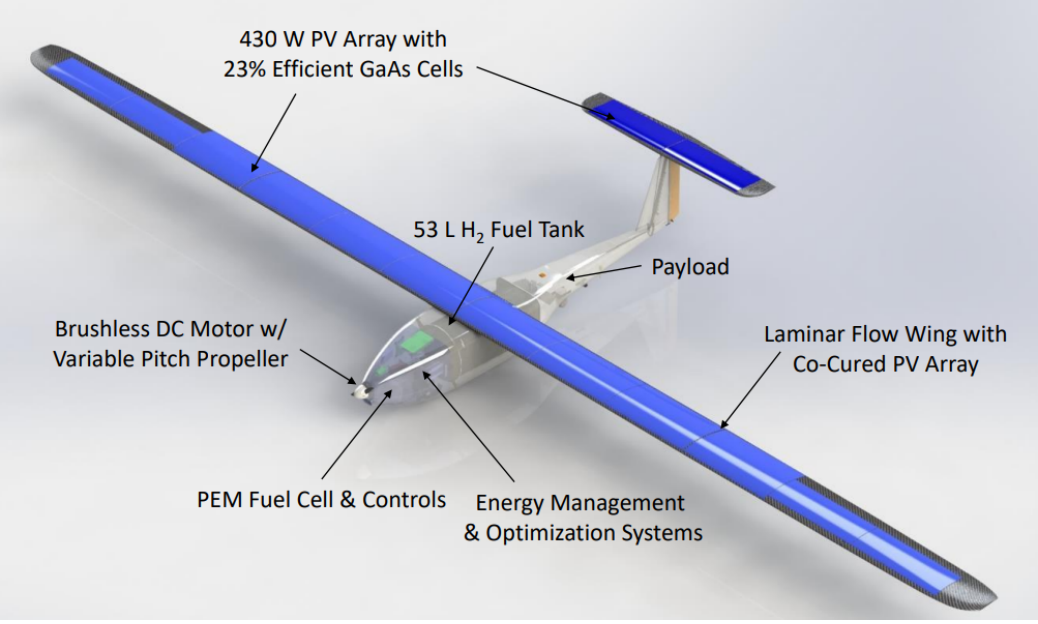

Figure 1.1. Hybrid Tiger Vehicle Design [2]

The Hybrid Tiger, shown in Figure 1.1, is a Group II UAS developed by the U.S. Naval Research Laboratory as a technology demonstrator. It combines a unique power plant, a soaring algorithm, and energy-optimal guidance to achieve the range and endurance benefits of these technologies integrated together. The Hybrid Tiger utilizes a hydrogen-electric propulsion suite, which, in combination with the solar arrays embedded in the wings, allows for energy harvesting in flight. Leveraging the specific energy gains from soaring and the electric energy gains from the solar arrays, the Hybrid Tiger autonomously manages the aircraft's energy to avoid consuming its H_2 fuel. Additionally, when it utilizes hydrogen fuel, the energy density of hydrogen combined with the high endurance design of the airframe

results in the fuel burn rate being only about 9 grams H_2 per hour. Finally, its energy-optimal path planning balances finding favorable weather and solar harvesting conditions by reducing cloud cover and orientation of solar arrays to the sun, and progressing towards the destination. Through all of these advancements, the Hybrid Tiger aircraft was able to fly routes that would be considered infeasible by "great circle" path planning to achieve multiple-day endurance.

1.3.2 Vanilla UAS — Prototype UAS

Figure 1.2. Vanilla above Pacific Ocean during UxS IBP 21 [3]

Vanilla UAS, shown in Figure 1.2, is a Group III UAS developed by Platform Aerospace and sponsored by the Office of Naval Research, Naval Air Systems Command, and NASA. It is powered by an internal combustion engine compatible with Jet-A fuel. During a test flight at Edwards Air Force Base, which began on 24 September 2021, Vanilla Unmanned flew continuously for 8 days, 50 minutes, and 47 seconds without refueling. During this

demonstration, it covered a distance of 12,200 miles [4]. There are two primary ways in which Vanilla has been able to achieve its outstanding performance — an airframe engineered for high endurance and a unique propulsion system. The aircraft's wings have been designed with an incredibly high aspect ratio, allowing for efficient lift generation. Additionally, all systems have been carefully scrutinized for weight savings, decreasing the required lift and thus reducing drag. The designed cruise velocity ensures that the wing operates in laminar flow, further reducing drag. The propulsion system utilizes a variable-pitch propeller driven by a reciprocating engine. An optimization loop is used to vary the engine speed and propeller pitch in order to generate the required thrust in the most fuel-efficient manner. From its innovative design, Vanilla has continuously stretched the horizons of what ultra-long endurance UAS are capable of.

1.4 Previous Work

This thesis builds on the thesis done by Shawn Lee titled "Energy Optimal Trajectory Planning of Long-Endurance UAV in Time-Varying Energy Fields" [5]. Lee's thesis solved the time-minimization and energy-minimization problem in "3-Dimensions" — lateral position, longitudinal position, and time — by using Pontryagin's Minimum Principle on a dynamics model tailored to Hybrid Tiger. In this thesis, the work done by Lee is considerably extended by incorporating fuel burn dynamics and altitude dynamics into the model.

Due to the unique power plant of the Hybrid Tiger UAS, a constant mass assumption was utilized. The solar arrays and lithium-ion batteries are a fixed mass of the aircraft. Additionally, the mass fraction of the hydrogen fuel was low ($\approx 5\%$). This, combined with the incredibly high energy density of hydrogen (120 MJ/kg which is about 3 times that of gasoline), resulted in a negligible change in mass throughout a flight profile flown by Hybrid Tiger. However, in order to extend the applicability of the previous research to the broader class of ultra-long endurance aircraft, fuel burn dynamics are discussed and incorporated into the model developed here.

Previously, most work has been able to ignore altitude dynamics by imposing a level-flight assumption and discretizing fixed-altitude slices around the desired cruise altitude, then calculating the optimal trajectory at each slice. However, by relaxing the level-flight assumption, the effects of air density gradients and vertical wind components are incorpo-

rated, resulting in a more efficient model. The incorporation of altitude dynamics into the model does result in a significant impact on the optimal trajectory planning of ultra-long endurance UAS, as frequently, the optimal trajectory involves changes in altitude. The results obtained from this proposed model will also show that the optimal trajectory often results in the UAS gliding between the most beneficial atmospheric effects. Additionally, the incorporation of altitude allows for 3-D obstacle avoidance, climbing, and updraft cases to be solved.

1.5 Tactical Implications for ISR Operations

The emergence of ultra-long endurance UAS represents a paradigm shift in the way that unmanned aerial systems are thought about. Considering that Vanilla UAS has demonstrated over 8 days of continuous flight without refueling suggests that future aircraft of this class have unprecedented potential for continuous and persistent surveillance over strategic regions. For example, Figures 1.3 and 1.4 show the coverage that Vanilla UAS can provide over strategic waterways in the Middle East and the western Pacific. These exceptional capabilities begin to blur the lines between conventional aircraft and reconnaissance satellites, offering the persistence and coverage of a satellite, with the responsiveness and flexibility of a traditional aircraft — being able to exchange sensor packages for different mission sets and roll out upgrades over time. This will make them invaluable assets in dynamic areas of operations where real-time intelligence is vital, providing enhanced situational awareness and enabling rapid decision-making.

However, many of the same factors that help enable the extreme endurance of these platforms also result in substantial susceptibility to hostile action. This partially arises from their slow air speeds, which makes them sitting targets for adversaries. Furthermore, any susceptibility or vulnerability reduction techniques necessitate the addition of weight, which as a consequence has a negative compounding effect on the UAS's time on station — the key performance parameter that makes this class of aircraft unique. As a result, ultra-high endurance UAS will likely have to be considered attritable assets when deployed in contested airspaces.

Though, ultra-long endurance UAS also brings improvements to the logistics of aircraft operation. The high fuel efficiency brings down the per-hour operating cost. Fewer cycles

are registered on the airframes for the long durations of required coverage. There are also fewer required hand-offs for continuous coverage, allowing for better data continuity. Additionally, there is a decreased likelihood of failing a hand-off. In the case of unexpected maintenance delays of aircraft on the ground, commanders are given more time to react.

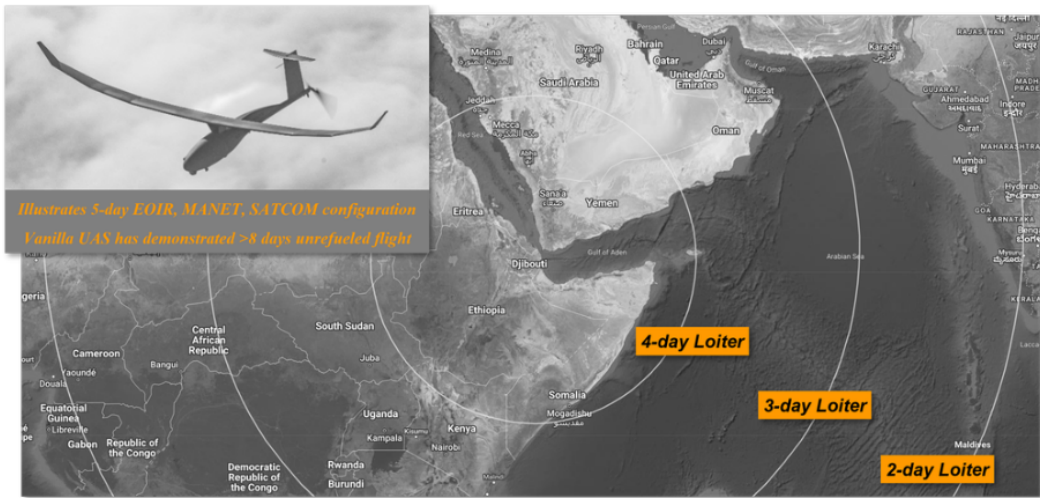

Figure 1.3. Vanilla Effective Radius — 5th Fleet Interest Area [6]

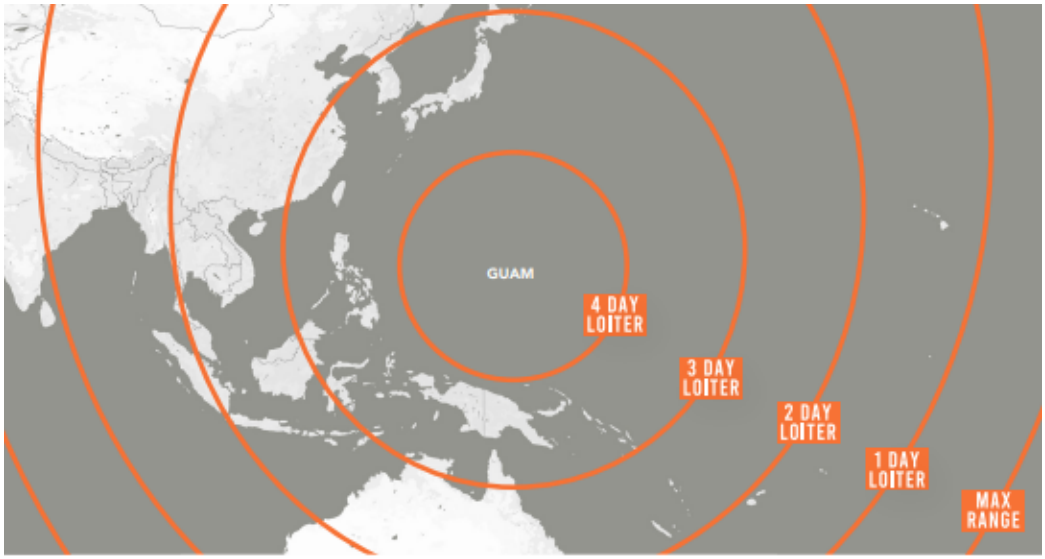

Figure 1.4. Vanilla Effective Radius — 7th Fleet Interest Area [7]

1.6 Thesis Outline

Chapter 1 introduces the goal of generating energy-optimal trajectories and discusses its applicability to the Department of Defense. It reviews some previous work in this field. It contextualizes the most applicable class of aircraft — Ultra-Long Endurance UAS — by discussing the Hybrid Tiger and Vanilla UAS. It then provides operational considerations and further justification for this work.

Chapter 2 develops the coupled mathematical model of aircraft dynamics and the energy (fuel mass) cost associated with its flight. It derives the cost function, state dynamics, and necessary constraints. It compiles all of this into the minimum energy problem statement. Finally, it discusses using aircraft flight test data to define some aircraft parameters and the constants in the cost function.

Chapter 3 describes the application of Pontryagin's minimization principle. First, the Lagrangian of the Hamiltonian is defined and the complementary conditions resulting from the path constraints are analyzed. The adjoint equations and stationary conditions are then derived and discussed. Finally, this chapter discusses the Hamiltonian Value Condition and Hamiltonian Evolution Equation.

Chapter 4 works through preliminary DIDO implementation. It works through the process of scaling and making algebraic modifications to the cost function and mass state to improve the quality of the results. The minimum energy problem statement and necessary conditions for optimality are updated. Verification and validation are conducted by checking feasibility via a propagation test and then checking that the necessary conditions are met.

Chapter 5 highlights the flexibility of the 3-dimensional minimum energy problem formulation by solving for trajectories in different scenarios. These are the updraft case, terrain-avoidance case, and time-varying wind case.

Chapter 6 provides the conclusion to this thesis. It reflects on the significance of the work completed before discussing potential future work.

CHAPTER 2:
Development of UAV Model and Optimal Control Problem Statement

In this chapter, the mathematical underpinnings of high endurance UAS are developed by the construction of a cost function for an aircraft flying in 3-dimensional space through a time-varying wind field. The cost function provides a clear understanding of what states, controls, and constraints are required to parameterize the system. Based on this, the minimum energy problem statement is composed. However, as the real world is more complex than this idealized model, the impact of edge cases and real-world factors are discussed. Finally, the model is verified and refined using real-world flight test data.

2.1 Cost Function — Power Required

To minimize the energy required over a flight profile, the time-integrated power required to maintain flight at a demanded velocity and attitude is decided as the cost function to be minimized. Thus, a function modeling the power required must be derived. This derivation begins with an examination of the four fundamental forces of steady flight and their corresponding orientation with respect to various frames of reference.

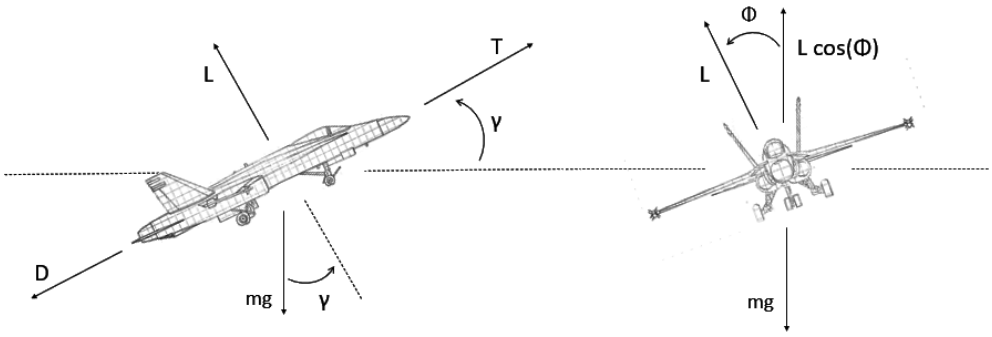

Figure 2.1. The Four Fundamental Forces of Flight on an Aircraft

Figure 2.1 displays a free-body diagram of an aircraft in flight. By assuming the engine's

thrust has no offset angle so that thrust aligns with the roll axis, the translational dynamics can be written as

$$m\dot{V}_a = T - D - W\sin(\gamma). \tag{2.1}$$

By assuming steady flight conditions ($\dot{V}_a = 0$), the translational dynamics equation can be written in terms of the thrust required to maintain the given flight conditions.

$$T = D + W\sin(\gamma) \tag{2.2}$$

The steady flight equation is then substituted into the definition of power to give the power required to maintain the flight conditions, which is the cost to be minimized.

$$P_r = T\frac{V_a}{\eta} = (D + W\sin(\gamma))\frac{V_a}{\eta} \tag{2.3}$$

The steady flight condition assumption does not significantly impact the accuracy of the model. In cases where $\dot{V}_a > 0$, this will result in P_r being an under approximation, and when $\dot{V}_a < 0$, this will result in an over-approximation. During the long endurance flight, these two scenarios largely cancel each other out. Furthermore, in reality, it is not common for ISR UAS to undergo significantly varied acceleration during a flight profile.

However, as it stands, Equation (2.3) does not incorporate rolling motion. To incorporate the effects of roll on the required power, we analyze Figure 2.1, which depicts an aircraft in a coordinated turn. The force balance for a coordinated turn can be described as

$$L\cos(\phi) = W\cos(\gamma). \tag{2.4}$$

Since lift is a fundamental component of induced drag, the drag term in Equation (2.3) provides the opportunity to incorporate the bank angle into the cost function. First, Equation (2.4) must be written in terms of C_L.

$$C_L = \frac{2W}{V_a^2\rho S}\frac{\cos(\gamma)}{\cos(\phi)} \tag{2.5}$$

In the definition of drag, C_L is included in the induced drag term.

$$C_D = C_{D0} + KC_L^2 \tag{2.6}$$

In utilizing the drag coefficient to then symbolically solve for drag, the lift required to maintain flight and the bank angle can be incorporated into Equation (2.3). This results in the expression for power required.

$$P_r = V_a^3 \rho K_{p1} + \frac{W^2}{V_a \rho} \frac{\cos^2(\gamma)}{\cos^2(\phi)} K_{p2} + \frac{V_a W \sin(\gamma)}{\eta} \tag{2.7}$$

where

$$K_{p1} = \frac{S C_{Do}}{2\eta} \qquad K_{p2} = \frac{2K}{\eta S} \tag{2.8}$$

The full derivation of power required is included in Appendix A.1. It is important to note that this model does not incorporate the power required for the electronics and sensor packages — only the power required to fly the trajectory is modeled. The power draw from these systems is further discussed in Section 2.4.

An additional sanity check can be performed to build confidence in the validity of this derivation of power required. By setting the derivative of power with respect to the airspeed equal to zero, the airspeed which consumes the least power is found. If the steady level flight assumption is applied such that there is no pitch or roll ($\gamma = 0$, $\phi = 0$), the following equation results:

$$V_a^2 = \frac{2W}{\rho S} \sqrt{\frac{K_p}{3C_{D0}}} \tag{2.9}$$

The step-by-step process to reach Equation (2.9) is shown in Appendix A.2. This expression is commonly known as the airspeed for minimum power required [8].

2.2 States, Simulated Weather, and Constraints

Having determined the power required for steady flight, the next step is to develop the state dynamics of the UAS. This section will explore the modeling of fuel consumption, the dynamics of an aircraft in a coordinated turn, and a kinematic model for change in position. By developing a thorough understanding of these state dynamics, we can evaluate the needed constraints to properly bound the problem. Furthermore, the atmospheric model for density and the simulated wind is developed. With these foundational components in place, the optimal control problem statement can be defined.

2.2.1 Fuel Consumption

While ultra-long endurance aircraft have incredibly low fuel consumption rates, it is important to model the mass change over time to develop a robust flight planning algorithm. Even a relatively small change in the fuel consumption rate does have significant cumulative impacts on flight performance over an extended duration of the flight. For the same airframe, a heavier aircraft will require more airspeed to maintain a given altitude compared to a lighter one, and in the process burn more fuel. With the aircraft's weight being contained solely in the numerator of the power required, Equation (2.7), a greater weight always shall cause a cost penalty. This relationship can also be observed in the common equation for fuel consumption. For a turboprop aircraft, the following equation gives the fuel burn rate.

$$\dot{m} = -\mu_{SFC} \cdot P_r \tag{2.10}$$

However, rather than using a theoretical approach, if flight test data is available, it is possible to empirically define the change in mass as a function of commanded airspeed, attitude, and current mass.

$$\dot{m} = f(V_a, \gamma, \phi, m) \tag{2.11}$$

This allows for the model to be more accurately tailored to the aircraft of interest. This process and its effects are further detailed in Section 2.4.

2.2.2 Heading Angle

In this model, the heading angle will be solely governed by the roll control variable ϕ. To accomplish this, all heading changes are modeled as a coordinated turn — a turn where airspeed is adjusted as the aircraft banks in order to not cause a change in altitude.

$$\dot{\psi} = \frac{g}{V_a} \tan(\phi) \tag{2.12}$$

This has a significant influence on the energy efficiency of the trajectory. Since the speed must be increased to avoid a loss in altitude, the aircraft must consume more fuel. As this presents a high penalty for substantial bank angles, it is expected that the optimized trajectory will feature gentle bank angles.

2.2.3 Position Kinematics

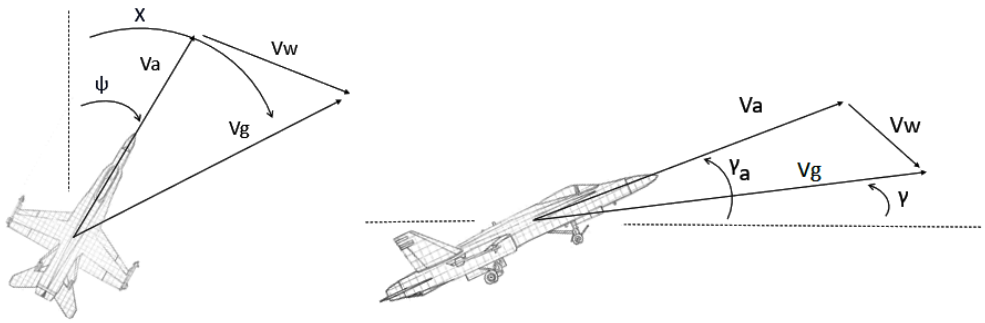

Figure 2.2. Definition of Wind Triangle

The first step in developing the model is establishing the connection between the control variables and the three position states. The air-relative velocity, inertial-relative velocity, and wind velocity, with their associated angles, are defined in Figure 2.2. While the aircraft's position and attitude, along with wind are in the Earth-fixed frame (NED), the true airspeed is given by the wind frame — the frame relating the aircraft's orientation and velocity to the wind vector through the angle of attack and the side slip angle.

$$V_g = V_a + V_w \tag{2.13}$$

Equation (2.13) relates the true airspeed and the speed of the wind to the ground speed. The wind triangle can then be expanded to vector form, however, this requires the use of two rotation matrices to present the true airspeed in the Earth-fixed frame.

$$\begin{bmatrix} \dot{x} \\ \dot{y} \\ \dot{h} \end{bmatrix} = V_a R + \begin{bmatrix} w_N \\ w_E \\ -w_D \end{bmatrix} \tag{2.14}$$

The first rotation takes place about the z axis. If the system is assumed to have no side slip ($\beta = 0$), as a good auto-pilot should be designed to be able to do, then part of this rotation is provided from the heading angle. The other rotation is by the climb angle relative to the

wind vector.

$$V_a R = \begin{bmatrix} \cos(\psi) & \sin(\psi) & 0 \\ \sin(\psi) & \cos(\psi) & 0 \\ 0 & 0 & 1 \end{bmatrix} \begin{bmatrix} \cos(\gamma_a) & 0 & \sin(\gamma_a) \\ 0 & 1 & 0 \\ -\sin(\gamma_a) & 0 & \cos(\gamma_a) \end{bmatrix} \begin{bmatrix} V_a \\ 0 \\ 0 \end{bmatrix} \tag{2.15}$$

Evaluating Equations (2.14) & (2.15) results in the position kinematic equations.

$$\dot{x} = V_a \cos(\psi) \cos(\gamma_a) + w_N \tag{2.16}$$

$$\dot{y} = V_a \sin(\psi) \cos(\gamma_a) + w_E \tag{2.17}$$

$$\dot{h} = V_a \sin(\gamma_a) - w_D \tag{2.18}$$

The sign of vertical wind in the altitude dynamic has been inverted to convert the dynamics to the NEU Earth-Fixed Frame. This is a choice made by the author for more intuitive verification and interpretation of the results.

2.2.4 Atmospheric Weather Model

Air Density

One of the strengths of building a model with altitude as a state is the ability to capture the vertical density gradient of the atmosphere. Air density plays a considerable role on the performance of the aircraft. With all other parameters held constant, a decrease in air density corresponds with a decrease in profile drag, an increase in induced drag, and a decrease in propeller efficiency. To approximate the density at altitude, an exponential function based on the 1976 U.S. Standard Atmosphere [9] is used.

$$\rho = 1.2245 e^{\frac{-h}{10400}} \quad (\frac{kg}{m^3}) \tag{2.19}$$

The strength of an exponential model is that its derivative with respect to altitude is easily calculated, smooth, and continuous — which facilitates numerical methods. However, this is a simple and idealized model, as in reality, air density varies with local weather systems.

Therefore, it can be more aptly written as a function of position and time.

$$\rho = f(x, y, h, t) \tag{2.20}$$

Utilizing a predictive weather model, like COAMPS [10] or HRRR [11], the density is obtained as a look-up table with a resolution of a couple of kilometers. However, in order to utilize this data in a numerical solving algorithm, a significant amount of pre-processing must be performed. Interpolation or a neural network can be used to produce intermediate values while ensuring continuous and smooth derivatives.

Wind

Many of the considerations with air density are equally applicable to modeling wind velocity. Wind velocity is a 3-dimensional array defined by position and time.

$$w = f(x, y, h, t) \tag{2.21}$$

However, to avoid pre-processing real-world data, in Chapter 4 and Chapter 5, idealized wind models are implemented. For ease of numerical solving, functions that provide constant or linear wind gradients are used. Pre-processing and tying real-world data into this model is further discussed in the future work Sections 6.1.1 and 6.1.2.

2.2.5 Development of Model Constraints

Multiple constraints are necessary to correctly pose the optimal control problem. These come from the physical relationship between problem variables, the intended operation of the aircraft, and aircraft design parameters.

Relating Air-Relative and Inertial-Relative Control Variables

The first path constraint is used to define the velocity in the inertial frame.

$$V_g = \sqrt{\dot{x}^2 + \dot{y}^2 + \dot{h}^2} \tag{2.22}$$

Substituting in the kinematics from Equations (2.16), (2.17), and (2.18) results in the first necessary path constraint to confine the control variables to their physical meaning.

$$h_1 := V_a^2 + V_w^2 - V_g^2 + 2V_a[\cos(\psi)\cos(\gamma_a)w_n + \sin(\psi)\cos(\gamma_a)w_e - \sin(\gamma_a)w_d] = 0 \quad (2.23)$$

The other required path constraint relates the wind-relative control variables to the inertial relative control variables. By definition, these variables are related by

$$V_a \sin(\gamma_a) = V_g \sin(\gamma). \quad (2.24)$$

By moving the variables to one side, the second path constraint is developed.

$$h_2 := \frac{V_a \sin(\gamma_a)}{V_g} - \sin(\gamma) = 0 \quad (2.25)$$

Altitude

The next path constraint creates a band of altitudes which the UAS is permitted to fly within. The lower bound is representative of a designated hard deck. The upper bound represents a service ceiling. Additionally, this constraint function can also be utilized to impose a vertical separation minimum on the aircraft.

$$h_3 := h_L \leq h \leq h_U \quad (2.26)$$

For most of this work, both bounds have been implemented as constant values. However, the result shown in Section 5.2 discusses utilizing this constraint for ground-avoidance by defining h_L as a function of ground position. Additionally, while not implemented, Section 6.1.3 discusses a more precise way of defining the upper bound.

Mass of the Aircraft

$$h_4 := m_e \leq m \quad (2.27)$$

The mass constraint is determined by the fuel capacity of the aircraft. The mass of the aircraft can not decrease below the fuel empty weight in flight, necessitating the inclusion of this constraint. This approach still holds if the aircraft is to release ordnance in flight, but

requires two optimal control problems to be solved in series. An example of how to set that up is shown in Appendix A.3.

Power Available

$$h_5 := P_{min} \leq P_r \leq P_{max} \tag{2.28}$$

The final constraint is a box constraint determined by the power plant of the aircraft. This constraint is much more powerful than it may appear at first glance. Because the power required is a function of attitude, altitude, and airspeed, it functions as the constraint for all of those parameters. From two values that are known values for an aircraft, a constraint for three controls and a state are created. This lets the solver have essentially "flexible" constraints on those parameters. For example, if the airspeed is high, this constraint will tighten the available climb angle.

2.3 Minimum Energy Problem Statement

Incorporating all of the equations developed in this chapter, the trajectory optimization problem for a minimum energy flight is formulated. By minimizing power, the minimum energy trajectory is found, since the integral of power is energy.

Minimize

$$J[X(\cdot), U(\cdot)] = \int_{t_0}^{t_f} \left(V_a^3 \rho K_{p1} + \frac{W^2}{V_a \rho} \frac{\cos^2(\gamma)}{\cos^2(\phi)} K_{p2} + \frac{V_a W \sin(\gamma)}{\eta} \right) dt, \tag{2.29}$$

on domain

$$X \in \mathbb{R}^6 \quad U \in \mathbb{R}^5,$$

where

$$X = \begin{bmatrix} x \\ y \\ h \\ \psi \\ m \\ t \end{bmatrix} \qquad U = \begin{bmatrix} V_a \\ \gamma \\ \phi \\ V_g \\ \gamma_a \end{bmatrix}, \tag{2.30}$$

subject to

$$\dot{x} = V_a \cos(\psi)\cos(\gamma_a) + w_N, \tag{2.31}$$

$$\dot{y} = V_a \sin(\psi)\cos(\gamma_a) + w_E, \tag{2.32}$$

$$\dot{h} = V_a \sin(\gamma_a) - w_D, \tag{2.33}$$

$$\dot{\psi} = \frac{g}{V_a}\tan(\phi), \tag{2.34}$$

$$\dot{m} = f(V_a, \gamma, \phi, m), \tag{2.35}$$

$$\dot{t} = 1, \tag{2.36}$$

with boundary conditions

$$m(t_0) = m_0, \tag{2.37}$$

$$x(t_0) = x_0 \quad x(t_f) = x_f, \tag{2.38}$$

$$y(t_0) = y_0 \quad y(t_f) = y_f, \tag{2.39}$$

$$z(t_0) = z_0 \quad z(t_f) = z_f, \tag{2.40}$$

$$t(t_0) = 0, \tag{2.41}$$

and path constraints

$$h_1 := V_a^2 + V_w^2 - V_g^2 + 2V_a(\cos(\psi)\cos(\gamma_a)w_n + \sin(\psi)\cos(\gamma_a)w_e - \sin(\gamma_a)w_d) = 0, \tag{2.42}$$

$$h_2 := \frac{V_a \sin(\gamma_a)}{V_g} - \sin(\gamma) = 0, \tag{2.43}$$

$$h_3 := h_L \leq h \leq h_U, \tag{2.44}$$

$$h_4 := m_e \leq m, \tag{2.45}$$

$$h_5 := P_{min} \leq P_r \leq P_{max}. \tag{2.46}$$

2.4 Translating Theory into Application

Translating engineering models to real-life systems is never as simple as the theory may suggest. Many parameters that are often assumed to be constants are not truly constant

in reality. This is where real-life test data from an aircraft can be used to improve the model to be more accurate to the aircraft it seeks to describe. This section demonstrates the process of tuning the constants in a model using actual test data from an aircraft. This data is not specifically from either Hybrid Tiger or Vanilla UAS but is shown as a method of demonstrating how its specifications can be arrived at via flight tests. Additionally, a discussion of how data can be used to estimate the fuel burn rate effectively is presented. Given below, Equations (2.47) and (2.48) show the values which have been assumed to be constants, but in fact are not, in bold. Additionally, while neglected to this point in the analysis, the power draw from the aircraft's electronics must also be incorporated.

$$P_r = V_a^3 \rho \mathbf{K_{p1}} + \frac{W^2}{V_a \rho} \frac{\cos^2(\gamma)}{\cos^2(\phi)} \mathbf{K_{p2}} + \frac{V_a W \sin(\gamma)}{\eta} + \mathbf{P_{gen}} \tag{2.47}$$

where

$$K_{p1} = \frac{S \mathbf{C_{Do}}}{2\boldsymbol{\eta}} \qquad K_{p2} = \frac{2\mathbf{K}}{\boldsymbol{\eta} S} \tag{2.48}$$

The zero-lift drag constant and drag polar constant vary based on the chosen mission and required payload packages. Additionally, the efficiency of the propeller changes with propeller pitch and rpm, which are directly impacted by the weight of the packages required for a mission. As the weight of the aircraft decreases over time via fuel consumption, the propulsion efficiency increases. Next, onboard electronics have a constant base power draw, with additional power required while in operation. For some systems, like active sensors, this power draw is considerably higher than its base usage when the sensor is utilized. Since these are not constant, it is important to approximate them in such a way that the error of assuming them to be constant is not biased in any way. The first step in doing this is to evaluate the lift and drag data provided by the aircraft.

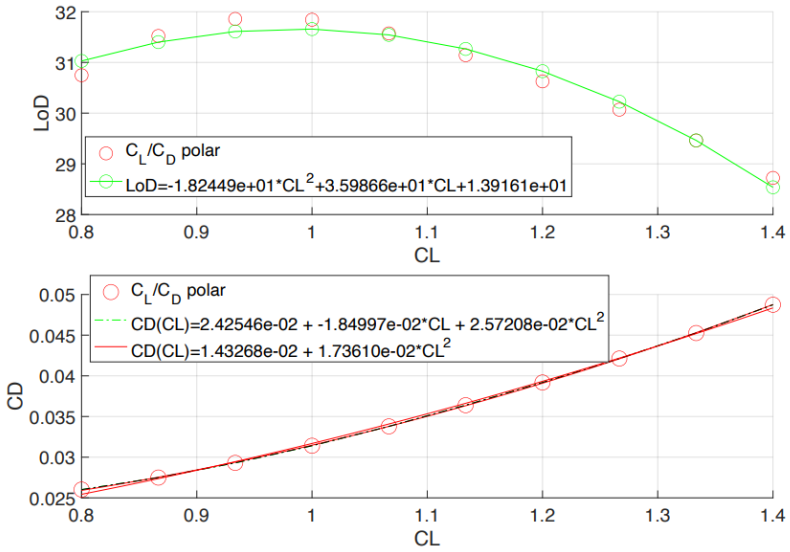

Figure 2.3. Interpolating Lift and Drag Data

From the lift and drag data of the aircraft, a quadratic polynomial interpolation may be applied to the drag polar data. To start relating this to the model, first turn to the definition of the zero-lift drag constant and drag polar constant.

$$C_D = C_{D0} + KC_L^2 \tag{2.49}$$

Through this conventional definition, there is no bC_L term in the quadratic polynomial fit, so another fit is performed where $b = 0$. Figure 2.3 shows that the result still well fits the data, thus providing the refined estimates for those two constants.

$$C_{D0} = 0.0143 \qquad K = 0.0174 \tag{2.50}$$

These values can be used as shown in Section 4.2.1 to calculate the aircraft cruise velocity — used to scale the velocity states. The next step is to refine the estimate for propulsive efficiency and electronic power requirements.

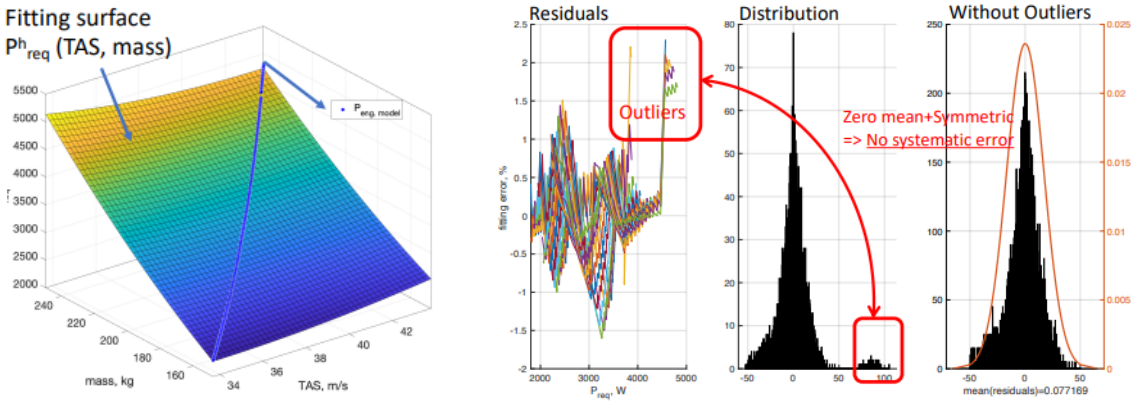

(a) Fitting Model (b) Statistical Analysis

Figure 2.4. P_{req} Fitting Results

Subfigure 2.4a represents the power required as a function of mass and true airspeed. The surface is generated from the truth model of the aircraft. However, the complexity of truth models makes them unsuitable for optimal control solvers as it does not allow for quick sampling. To use the truth model to refine this paper's model, a flight profile is fit to the surface. This is represented by the blue line of Subfigure 2.4a. From there, comparing the fit to the truth model allows for the quantification of the error. This error and the distribution of its values are shown in Subfigure 2.4b. By removing the outliers that appear at max power, the data becomes a normal distribution. This allows for the mean to be used as the estimate for the power required constants, without any bias in the error.

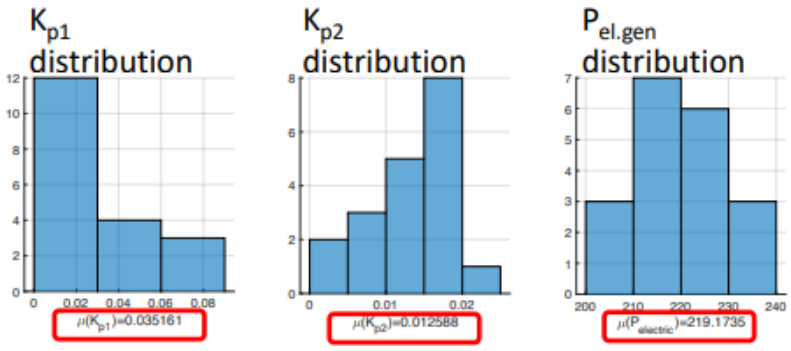

Figure 2.5. Resulting Estimates for K_{p1}, K_{p2}, and P_{gen}

With the error normalized, the values of the power constants can be estimated. Figure 2.5 shows the resulting histogram of values for the zero-lift drag constant, drag polar constant, and power generation. Taking the mean results in the final estimates for these values.

$$K_{p1} = 0.0352 \tag{2.51}$$

$$K_{p2} = 0.0126 \tag{2.52}$$

$$P_{gen} = 219.17 \quad (W) \tag{2.53}$$

2.5 Hybrid Tiger Specifications

All of the results in this thesis will use aircraft parameters that model the Hybrid Tiger. The aircraft will be operating solely on Hydrogen fuel, neglecting electrical energy gains from the solar arrays and lithium-ion batteries. From the same process as demonstrated in Section 2.4, the zero-lift drag constant and drag polar constant can be found.

$$K_{p1} \approx 0.034 \quad (m^2) \tag{2.54}$$

$$K_{p2} \approx 0.016 \quad (\frac{1}{m^2}) \tag{2.55}$$

Next, we must define the fuel burn dynamic equation. A polynomial model for the Hybrid Tiger prototype UAS has been provided for use.

$$\dot{m} = [c_1 P_r^2 + c_2 P_r + c_3] \quad (\frac{g}{hr}) \tag{2.56}$$

where

$$c_1 = 3.35e{-}5 \quad (\frac{g}{W^2 hr}) \tag{2.57}$$

$$c_2 = 4.19e{-}2 \quad (\frac{g}{W hr}) \tag{2.58}$$

$$c_3 = 8.06e{-}1 \quad (\frac{g}{hr}) \tag{2.59}$$

$$\tag{2.60}$$

There are two more constants that must be defined for the model— the weight [2] and propulsion efficiency. An estimate of 0.85 is used for propulsion efficiency.

$$m_0 = 23.93 \quad (kg) \tag{2.61}$$

$$\eta = 0.85 \tag{2.62}$$

Finally, two of the path constraints are defined by the aircraft's specification. Of the two, the first defines the fuel fraction of the aircraft. For the Hybrid Tiger, only 5% of the aircraft mass is fuel [2]. The other path constraint is the power required. The upper bound is an estimate of the max power output of the Hybrid Tiger, while the lower bound represents the aircraft on a glide slope.

$$h(x)_4 := 22.73 \leq m \quad (kg) \tag{2.63}$$

$$h(x)_5 := 0 \leq P_r \leq 475 \quad (W) \tag{2.64}$$

By defining all of these parameters, the solver will have all the information required to find energy-optimal trajectories for the Hybrid Tiger.

2.6 Chapter Summary

This chapter derived and discussed all equations required to model an ultra-long endurance UAS in 3-Dimensions and time. First, the power required was set as the running cost and subsequently derived. Then, all other functions governing the state variables, atmospheric effects, and path constraints were established, culminating in the energy-optimal problem formulation. Real-world data was shown in a demonstration of how flight test data can be utilized to establish aircraft constants, before the introduction of the Hybrid Tiger's relevant specifications. With all of these components established, Pontryagin's Minimum Principle can now be applied to the problem.

THIS PAGE INTENTIONALLY LEFT BLANK

CHAPTER 3:
Evaluating the Boundary Value Problem

This chapter analyzes the boundary value problem resulting from the application of Pontryagin's Minimization Principle to the optimal-control problem formulation. First, the Hamiltonian is constructed. Then, after incorporating the path constraints to create the Lagrangian of the Hamiltonian, the complementary conditions are analyzed for their behavior when path constraints are active. Next, the definition of the costate dynamics, Hamiltonian minimization condition, transversality conditions, Hamiltonian Evolution Equation, and Hamiltonian Value Condition are evaluated.

3.1 Hamiltonian

The Hamiltonian for the optimal control problem formulation is defined as the dot product between a costate vector and the state dynamics summed with the running cost.

$$H = F + \lambda^T f \tag{3.1}$$

Thus, using the model developed in Chapter 2, the Hamiltonian for the energy-optimal control task is

$$\begin{aligned} H = V_a^3 \rho K_{p1} + \tfrac{W^2}{V_a \rho} \tfrac{\cos^2(\gamma)}{\cos^2(\phi)} K_{p2} + \tfrac{V_a W \sin(\gamma)}{\eta} + \lambda_x (V_a \cos(\psi)\cos(\gamma_a) + w_N) \\ +\lambda_y (V_a \sin(\psi)\cos(\gamma_a) + w_E) + \lambda_h (V_a \sin(\gamma_a) - w_D) + \lambda_\psi (\tfrac{g}{V_a}\tan(\phi)) \\ +\lambda_m \dot{m} \end{aligned} . \tag{3.2}$$

3.1.1 Lagrangian of Hamiltonian

The Lagrangian of the Hamiltonian incorporates the path constraints discussed in Section 2.2.5. This is constructed as

$$\bar{H} = H + \mu^T h. \tag{3.3}$$

Now, it is possible to examine the complementary conditions [12], which give insight into the behavior of μ. The first two constraints, h_1 and h_2, are equality constraints, so they are

always active. This results in μ_1 and μ_2 being unrestricted in value and sign.

$$\mu_1 = \left\{ \text{unrestricted} \right. \tag{3.4}$$

$$\mu_2 = \left\{ \text{unrestricted} \right. \tag{3.5}$$

The next path constraint is the box constraint placed on the aircraft's altitude. Covariable μ_3 is zero unless the aircraft altitude constraint is active. When the constraint is active, μ_3 takes a value according to

$$\mu_3 = \begin{cases} \leq 0 & \text{if} \quad h = h_L \\ = 0 & \text{if} \quad h_L < h < h_U \\ \geq 0 & \text{if} \quad h = h_U \end{cases} . \tag{3.6}$$

The mass constraint should not be active during the trajectory. Otherwise, it is indicating that the aircraft has run out of fuel. This would suggest that the boundary conditions, as specified, are infeasible and the aircraft does not have the necessary fuel to complete the trajectory. So it is anticipated that $\mu_4 = 0$ for a feasible solution.

$$\mu_4 = \begin{cases} \leq 0 & \text{if} \quad m = m_e \\ = 0 & \text{if} \quad m < m_e \end{cases} \tag{3.7}$$

Finally, the complementary condition on the power required is likely to be activated during most trajectories. The upper bound is activated when the aircraft is at full power. On the other side, the lower bound is active when the aircraft is on a glide slope. The following equation dictates the behavior of μ_5.

$$\mu_5 = \begin{cases} \leq 0 & \text{if} \quad P_r = P_{min} \\ = 0 & \text{if} \quad P_{min} < P_r < P_{max} \\ \geq 0 & \text{if} \quad P_r = P_{max} \end{cases} \tag{3.8}$$

3.2 Adjoint Equations

The adjoint equations define the time behavior of the covector. They are calculated by taking the derivative of the negative Lagrangian of the Hamiltonian with respect to the state variables.

$$\dot{\lambda} = -\frac{\partial \bar{H}}{\partial X} \tag{3.9}$$

The adjoint equations not only define the covector but also play an important role in the verification and validation (V&V) of results. The computed results must obey the adjoint equations for the candidate solution to be considered optimal. Some equations are simple enough to gain some intuition about the behavior of particular costates. However, some of the results are too complicated and will require computer graphing to conduct V&V. The adjoint equations are now developed.

$$\dot{\lambda_x} = -\frac{\partial \bar{H}}{\partial x} = -\lambda_x \frac{\partial w_N}{\partial x} - \lambda_y \frac{\partial w_E}{\partial x} + \lambda_h \frac{\partial w_D}{\partial x} \tag{3.10}$$

If the wind is constant with respect to x, the costate of x, λ_x, is constant.

$$\dot{\lambda_y} = -\frac{\partial \bar{H}}{\partial y} = -\lambda_x \frac{\partial w_N}{\partial y} - \lambda_y \frac{\partial w_E}{\partial y} + \lambda_h \frac{\partial w_D}{\partial y} \tag{3.11}$$

Similarly, if the wind is constant with respect to y, the costate of y, λ_y, is constant.

$$\dot{\lambda_h} = -\frac{\partial \bar{H}}{\partial h} = -\frac{\partial P_r}{\partial h} - \lambda_x \frac{\partial w_N}{\partial h} - \lambda_y \frac{\partial w_E}{\partial h} + \lambda_h \frac{\partial w_D}{\partial h} - \lambda_m \frac{\partial \dot{m}}{\partial h} - \mu_3 - \mu_5 \frac{\partial P_r}{\partial h} \tag{3.12}$$

where

$$-\frac{\partial P_r}{\partial h} = -V_a^3 \frac{\partial \rho}{\partial h} K_{p1} - \frac{m^2 g^2}{V_a} \frac{\cos^2(\gamma)}{\cos^2(\phi)} K_{p2} \frac{\partial}{\partial h}\left(\frac{1}{\rho}\right) \tag{3.13}$$

The costate of altitude is governed by the most complex equation. In addition to dependence on the wind, it is also affected by the altitude dependence of atmospheric density — both in the cost component of the Hamiltonian and the power required constraint in the Lagrangian — and μ_3 via the altitude constraint. Additionally, depending on the fuel burn model used, the partial derivative of mass with respect to altitude may be non-zero and need to be included.

$$\dot{\lambda_\psi} = -\frac{\partial \bar{H}}{\partial \psi} = \lambda_x V_a \sin(\psi)\cos(\gamma_a) - \lambda_y V_a \cos(\psi)\cos(\gamma_a) \tag{3.14}$$

The costate of the heading angle is solely defined by the derivatives of the ground track dynamics and their respective costates.

$$\dot{\lambda_m} = -\frac{\partial \bar{H}}{\partial m} = -\frac{\partial P_r}{\partial m} - \lambda_m \frac{\partial \dot{m}}{\partial m} - \mu_4 - \mu_5 \frac{\partial P_r}{\partial m} \tag{3.15}$$

where

$$-\frac{\partial P_r}{\partial m} = -\frac{2mg^2}{V_a \rho} \frac{\cos^2(\gamma)}{\cos^2(\phi)} K_{p2} - \frac{V_a g \sin(\gamma)}{\eta} \tag{3.16}$$

The mass costate is heavily influenced by the partial derivative of the power required with respect to mass, as P_r appears in the running cost, power constraint, and the fuel burn model. Additionally, μ_4 is included, but as discussed in Section 3.1.1, is expected to be 0 during flight.

$$\dot{\lambda_t} = -\frac{\partial \bar{H}}{\partial t} = -\lambda_x \frac{\partial w_N}{\partial t} - \lambda_y \frac{\partial w_E}{\partial t} + \lambda_h \frac{\partial w_D}{\partial t} \tag{3.17}$$

Finally, the time costate only depends on the time dependence of the wind. If the wind is constant in time, λ_t is constant.

3.3 Hamiltonian Minimization Condition

Pontryagin's Minimization Principle states that the partial derivative of the Lagrangian of the Hamiltonian with respect to the control variables shall be zero for all time in the optimal solution. That is

$$\frac{\partial \bar{H}}{\partial U} = 0. \tag{3.18}$$

Checking that this holds true is an important component in finding optimal controls and validating solutions. Additionally, it is necessary to use these equations to solve for the control variable for some numerical methods. However, this is not conducted for the airspeed, inertial-frame climb angle, and bank angle. This is because each of those control variables is part of the power required, which is directly tied to the fuel burn dynamics. Because different fuel burn models can be used, like neural networks and different order polynomial interpolations, the components due to the fuel model is left as $\frac{\partial \dot{m}}{\partial U}$. While being more broadly applicable, it does not allow the control variables that influence the fuel burn model to be specifically isolated.

3.3.1 Aircraft Velocity (Air Relative)

The airspeed appears in many parts of the cost function, dynamics, and path constraints.

$$\begin{aligned}\frac{\partial \bar{H}}{\partial V_a} = \frac{\partial P_r}{\partial V_a} + \lambda_x \frac{\partial \dot{x}}{\partial V_a} + \lambda_y \frac{\partial \dot{y}}{\partial V_a} + \lambda_h \frac{\partial \dot{h}}{\partial V_a} + \lambda_\psi \frac{\partial \dot{\psi}}{\partial V_a} + \lambda_m \frac{\partial \dot{m}}{\partial V_a} \\ +\mu_1 \frac{\partial h_1}{\partial V_a} + \mu_2 \frac{\partial h_2}{\partial V_a} + \mu_5 \frac{\partial h_5}{\partial V_a} = 0\end{aligned} \tag{3.19}$$

Substituting all of the components results in the most complex of the Hamiltonian minimization conditions.

$$\begin{aligned}\frac{\partial \bar{H}}{\partial V_a} = (3V_a^2 \rho K_{p1} - \frac{m^2 g^2}{V_a^2 \rho} \frac{\cos^2(\gamma)}{\cos^2(\phi)} K_{p2})(1+\mu_5) + \frac{mg\sin(\gamma)}{\eta} + \lambda_x \cos(\psi)\cos(\gamma_a) \\ +\lambda_y \sin(\psi)\cos(\gamma_a) + \lambda_h \sin(\gamma_a) - \lambda_\psi \frac{g}{V_a^2}\tan(\phi) + \lambda_m \frac{\partial \dot{m}}{\partial V_a} \\ +\mu_1(2V_a + 2(\cos(\psi)\cos(\gamma_a w_n + \sin(\psi)\cos(\gamma_a) w_e - \sin(\gamma_a) w_d))) \\ +\mu_2 \frac{\sin(\gamma_a)}{V_g} + \mu_5 = 0\end{aligned} \tag{3.20}$$

There is not much that can be intuitively drawn from an equation this complex. However, can be evaluated after running a solution to verify the results, namely that when the solution data is substituted in, a zero curve results.

3.3.2 Climb Angle (Inertial Relative)

The inertial-relative climb angle appears in the cost function, fuel burn model, and fifth path constraint through its inclusion in the power required. It also appears in the second path constraint, which defines the relationship between the two frames.

$$\frac{\partial \bar{H}}{\partial \gamma} = \frac{\partial P_r}{\partial \gamma} + \lambda_m \frac{\partial \dot{m}}{\partial \gamma} + \mu_2 \frac{\partial h_2}{\partial \gamma} + \mu_5 \frac{\partial h_5}{\partial \gamma} = 0 \tag{3.21}$$

The partial derivatives are evaluated as

$$\frac{\partial \bar{H}}{\partial \gamma} = (\frac{-2m^2 g^2}{V_a \rho} \frac{\sin(\gamma)\cos(\gamma)}{\cos^2(\phi)} K_{p2} + \frac{V_a mg}{\eta}\cos(\gamma))(1+\mu_5) + \lambda_m \frac{\partial \dot{m}}{\partial \gamma} - \mu_2 \cos(\gamma) = 0 \ . \tag{3.22}$$

Just like Equation (3.20), Equation (3.22) is too complex to draw any direct conclusions from — especially since μ_2 is unrestricted.

3.3.3 Bank Angle

The bank angle control variable is present only in the power required and heading angle equations.

$$\frac{\partial \bar{H}}{\partial \phi} = \frac{\partial \dot{P}_r}{\partial \phi} + \lambda_\psi \frac{\partial \dot{\psi}}{\partial \phi} + \lambda_m \frac{\partial \dot{m}}{\partial \phi} + \mu_5 \frac{\partial h_5}{\partial \phi} = 0 \tag{3.23}$$

Evaluating the partial derivatives in Equation (3.23) results in the first equation where some insight can be drawn.

$$\frac{\partial \bar{H}}{\partial \phi} = \frac{2m^2 g^2 \cos^2(\gamma)}{V_a \rho} \frac{\sin(\phi)}{\cos^3(\phi)} K_{p2}(1 + \mu_5) + \lambda_m \frac{\partial \dot{m}}{\partial \phi} + \lambda_\psi \frac{g}{V_a \cos^2(\phi)} = 0 \tag{3.24}$$

In a wings-level flight, $\phi = 0$, all of the terms arising from the power required equation are zero. Only the term resulting from the heading angle dynamics remains. The only way for that term to be zero is if the heading costate is zero. Therefore, for optimality in wings-level flight, $\lambda_\psi = 0$. This can be verified as part of validating the numerical solution.

3.3.4 Climb Angle (Air Relative)

The air-relative climb angle control variable is present in the position dynamics and the first two path constraints.

$$\frac{\partial \bar{H}}{\partial \gamma_a} = \lambda_x \frac{\partial \dot{x}}{\partial \gamma_a} + \lambda_y \frac{\partial \dot{y}}{\partial \gamma_a} + \lambda_h \frac{\partial \dot{h}}{\partial \gamma_a} + \mu_1 \frac{\partial h_1}{\partial \gamma_a} + \mu_2 \frac{\partial h_2}{\partial \gamma_a} = 0 \tag{3.25}$$

All of the above partial derivatives are then evaluated.

$$\begin{aligned} \tfrac{\partial \bar{H}}{\partial \gamma_a} = &-\lambda_x V_a \cos(\psi)\sin(\gamma_a) - \lambda_y V_a \sin(\psi)\sin(\gamma_a) + \lambda_h V_a \cos(\gamma_a) \\ &-2V_a \mu_1 (\cos(\psi)\sin(\gamma_a) w_n + \sin(\psi)\sin(\gamma_a) w_e + \cos(\gamma_a) w_d) \\ &+ \tfrac{V_a}{V_g} \mu_2 \cos(\gamma_a) = 0 \end{aligned} \tag{3.26}$$

From Equation (3.26), it is possible to isolate the air-relative climb angle.

$$\tan(\gamma_a) = \frac{\lambda_h - 2w_d \mu_1 + \frac{\mu_2}{V_g}}{\lambda_x \cos(\psi) + \lambda_y \sin(\psi) + 2\cos(\psi) w_n \mu_1 + 2\sin(\psi) w_e \mu_1} \tag{3.27}$$

Even in this form, Equation (3.27) is too complex to draw substantial initial conclusions from. It can be noted that γ_a cannot equal $\frac{\pi}{2}$, or the equation will become undefined.

However, there would be no expectation that an optimal solution would result in the aircraft being pitched vertically, so this observation is not particularly useful.

3.3.5 Aircraft Velocity (Inertial Relative)

The inertial relative velocity is only defined by the two path constraints which govern the relationship between frames.

$$\frac{\partial \bar{H}}{\partial V_g} = \mu_1 \frac{\partial h_1}{\partial V_g} + \mu_2 \frac{\partial h_2}{\partial V_g} = 0 \tag{3.28}$$

Taking the partial derivatives of the path constraints results in the simplest of the necessary conditions.

$$\frac{\partial \bar{H}}{\partial V_g} = -2\mu_1 V_g - \mu_2 \frac{V_a \sin(\gamma_a)}{V_g^2} = 0 \tag{3.29}$$

Like the previous section, this can also be written in terms of the control variable.

$$V_g^3 = -\frac{V_a \sin(\gamma_a)\mu_2}{2\mu_1} \tag{3.30}$$

This condenses to a nice concise synthesis of the optimal inertial velocity. However, since both μ_1 and μ_2 are unrestricted, no initial observations can be drawn.

3.4 Transversality Condition

The transversality condition supplies additional boundary conditions for the optimal control BVP in the case that states at the final time are unspecified. The first step is to construct the Endpoint Lagrangian.

$$\bar{E} = \nu_x e_x + \nu_y e_y + \nu_h e_h \tag{3.31}$$

Then, the Endpoint Lagrangian is differentiated with respect to each state variable to see if any new information is revealed. The final boundary conditions for the position states are known, so the transversality condition provides no additional information.

$$\lambda_x(t_f) = \frac{\partial \bar{E}}{\partial x_f} = \nu_x \tag{3.32}$$

$$\lambda_y(t_f) = \frac{\partial \bar{E}}{\partial y_f} = \nu_y \tag{3.33}$$

$$\lambda_h(t_f) = \frac{\partial \bar{E}}{\partial h_f} = \nu_h \tag{3.34}$$

However, this is only the case if a final altitude is specified. There could be a case where the desired final altitude is not specified, resulting in $\lambda_h(t_f) = 0$. The final values of the heading angle, mass, and time are not specified in the problem formulation, resulting in their respective costates being zero at the final time.

$$\lambda_\psi(t_f) = \frac{\partial \bar{E}}{\partial \psi_f} = 0 \tag{3.35}$$

$$\lambda_m(t_f) = \frac{\partial \bar{E}}{\partial m_f} = 0 \tag{3.36}$$

$$\lambda_t(t_f) = \frac{\partial \bar{E}}{\partial t_f} = 0 \tag{3.37}$$

Transversality conditions are easy to verify with respect to the numerical results.

3.5 Hamiltonian Value Condition

The Hamiltonian Value Condition provides the expected value of the Hamiltonian at the final time.

$$\bar{H}(t_f) = -\frac{\partial \bar{E}}{\partial t_f} = 0 \tag{3.38}$$

The optimal control task is neither time-fixed nor min-time, so the final state of the Hamiltonian shall be 0.

3.6 Hamiltonian Evolution Equation

If the wind does not vary with time, it is expected that the minimized Hamiltonian will remain constant in time. This is due to the wind being the only component of the Hamiltonian which is a function of time. With the atmosphere being incredibly dynamic, this is an over-idealized case. However, many of the test cases run do not incorporate time-varying wind so it does

provide information useful for the validation of results.

$$\frac{\partial \bar{H}}{\partial t} = \frac{d\bar{\mathcal{H}}}{dt} = 0 \tag{3.39}$$

If the wind is time dependent like in the case exhibited in Section 5.3, the Hamiltonian behavior shall vary with the time derivative of the wind and the position costates.

$$\frac{\partial \bar{H}}{\partial t} = \frac{d\bar{\mathcal{H}}}{dt} = \lambda_x \frac{\partial w_N}{\partial t} + \lambda_y \frac{\partial w_E}{\partial t} - \lambda_h \frac{\partial w_D}{\partial t} \tag{3.40}$$

By plotting the Hamiltonian given by the numerical solution, the Hamiltonian Evolution Equation and the Hamiltonian Evolution Equation are used to validate the results.

3.7 Chapter Summary

This chapter applies Pontryagin's Minimum Principle to the energy-optimal problem formulation developed in Chapter 2. The Lagrangian of the Hamiltonian is defined and subsequently, the complementary conditions are discussed. The adjoint equations, which govern the time behavior of the costates, are developed. The Hamiltonian is minimized with respect to the control variables. The transversality conditions are found by taking the derivative of the Endpoint Lagrangian with respect to the final states, resulting in the final-time boundary conditions for costates whose states have unspecified boundary conditions. The Hamiltonian Evolution Equation and Hamiltonian Value Condition provide the expected behavior of the Hamiltonian in the energy-optimal solution. All of these steps contribute to optimality checks and provide greater insight into the behavior of the system. The problem can now begin to be implemented in a numerical solver.

THIS PAGE INTENTIONALLY LEFT BLANK

CHAPTER 4:
Testing and Refining the Problem Formulation

With all the underlying theory developed, the subsequent task is to numerically solve the problem. This is accomplished using DIDO [12] — an external MATLAB toolbox. Unlike most numerical solving algorithms, DIDO does not require an initial guess [13], but instead operates off a user-provided search space for the state and control variables. This removes the need for an initialization algorithm to be developed. However, to facilitate the numerical process it is necessary to scale the problem [14]. Scaling is an iterative process. This chapter demonstrates this process by formulating the scaled problem statement, evaluating the results, and then refining the scaling. It then concludes by verifying and validating the obtained results to ensure the reliability and accuracy of the solution.

4.1 Defining the Problem

This first case will consider the Hybrid Tiger aircraft flying through a constant gradient wind field. The aircraft will be operating solely on Hydrogen fuel, neglecting electrical energy from the solar arrays and lithium-ion batteries. To define the problem, the constants, boundary values, and constraint parameters from the problem statement outlined in Section 2.3 must be assigned numerical values. These values primarily come from three categories of parameters: aircraft specifications, weather, and operator inputs. The aircraft specifications are shown in Section 2.5 and are restated below.

$$\eta = 0.85 \tag{4.1}$$

$$K_{p1} \approx 0.034 \quad (m^2) \tag{4.2}$$

$$K_{p2} \approx 0.016 \quad (\frac{1}{m^2}) \tag{4.3}$$

The polynomial fuel burn model is used.

$$\dot{m} = [c_1 P_r^2 + c_2 P_r + c_3] \quad (\frac{g}{hr}) \tag{4.4}$$

where

$$c_1 = 3.35e{-}5 \quad (\frac{g}{W^2 hr}) \tag{4.5}$$
$$c_2 = 4.19e{-}2 \quad (\frac{g}{Whr}) \tag{4.6}$$
$$c_3 = 8.06e{-}1 \quad (\frac{g}{hr}) \tag{4.7}$$
$$\tag{4.8}$$

The final aircraft-specific parameters are implemented in the path constraints.

$$h_4(x) = 22.73 \leq m \quad (kg) \tag{4.9}$$
$$h_5(x) = 0 \leq P_r \leq 475 \quad (W) \tag{4.10}$$

Next, the operator inputs are the boundary conditions and the altitude constraint. In this case, the aircraft is commanded to fly 10 km North and 10 km East. It originates and culminates its flight at an altitude of 3 km. There is no specified time at which it must arrive.

$$(t_0) = (0) \quad (s) \tag{4.11}$$
$$(x_0, x_f) = (0, 10) \quad (km) \tag{4.12}$$
$$(y_0, y_f) = (0, 10) \quad (km) \tag{4.13}$$
$$(h_0, h_f) = (3, 3) \quad (km) \tag{4.14}$$

Of the five constraints, recall that $h_1(x)$ and $h_2(x)$ define the physical relationship between the two reference frames. With $h_4(x)$ and $h_5(x)$ defined by the aircraft parameters, the only path constraint that needs to be specified is the altitude constraint, $h_3(x)$. Since the primary goal of this section is to refine the scaling, it has been set in such a way that it should not be active in this trajectory.

$$h_3(x) = 0 \leq h \leq 15000 \quad (m) \tag{4.15}$$

Finally, the environment must be defined. Gravity is defined as a constant value of $g = 9.815(\frac{m}{s^2})$. The wind field is chosen to be time-invariant and has a constant gradient.

$$w = [0, 3\bar{x}, 0]^T \quad (\frac{m}{s}) \tag{4.16}$$

Since the primary purpose of this first case is to work through the scaling, it is important to select a wind field that generates an intuitive result. The scaled variable $\bar{x}$ was utilized as it provides a wind field that varies from 0 to about 2 $\frac{m}{s}$ throughout the flight.

4.2 Initial Implementation

4.2.1 Scaling Factors

The objective of scaling is to normalize the problem variables such that their values remain within similar bounds, for example, vary from 0 to 1. One way to achieve this for positional states is by taking the Euclidean distance from the initial to the final position.

$$L = \sqrt{(x_f - x_0^2) + (y_f - y_0)^2 + (h_f - h_0)^2} \tag{4.17}$$

Since the mass is always decreasing, an intuitive way to scale it is based on the initial mass of the aircraft, so that the scaled mass is decreasing from 1.

$$M = m_0 \tag{4.18}$$

In Section 2.1, the cost function was used to derive the optimal airspeed for max endurance at steady and level flight. This serves as a good scaling factor as it will always be around 1.

$$V = \sqrt{\frac{2W}{\rho S}\sqrt{\frac{K_p}{3C_{D0}}}} \tag{4.19}$$

Finally, to keep units consistent, the scaling factor for time is established from the scaling factors for distance and velocity.

$$T = \frac{L}{V} \tag{4.20}$$

Thus, the scaled problem states are initially defined as

$$\bar{x} = \frac{x}{L}, \tag{4.21}$$

$$\bar{y} = \frac{y}{L}, \tag{4.22}$$

$$\bar{h} = \frac{h}{L}, \tag{4.23}$$

$$\bar{v} = \frac{v}{V} = \frac{T}{L}v, \tag{4.24}$$

$$\bar{t} = \frac{t}{T}, \tag{4.25}$$

$$\bar{m} = \frac{m}{M}. \tag{4.26}$$

Now, these scaling factors are applied to the state dynamics using these scaled states.

$$\dot{\bar{x}} = \frac{d(\frac{x}{L})}{d(\frac{t}{T})} = \frac{T}{L}\frac{dx}{dt} = (V_a \cos(\psi)\cos(\gamma_a) + w_N)\frac{T}{L} \tag{4.27}$$

And since $V = \frac{L}{T}$,

$$\dot{\bar{x}} = \frac{V_a}{V}\cos(\psi)\cos(\gamma_a) + \frac{w_N}{V}. \tag{4.28}$$

Similarly,

$$\dot{\bar{y}} = \frac{V_a}{V}\sin(\psi)\cos(\gamma_a) + \frac{w_E}{V}, \tag{4.29}$$

$$\dot{\bar{h}} = \frac{V_a}{V}\sin(\gamma_a) - \frac{w_D}{V}. \tag{4.30}$$

Since angles exist in $[-\pi, \pi]$, it is often not needed to scale them. As such, the heading angle is only scaled by the time scaling factor.

$$\dot{\bar{\psi}} = \frac{\partial\psi}{\partial t}T = \frac{gT}{V_a}\tan(\phi) \tag{4.31}$$

The fuel burn model is scaled using the scaling factors for time and mass.

$$\dot{\bar{m}} = \dot{m}(\frac{T}{M}) \tag{4.32}$$

The scaling factors for the power required are applied to correspond with the definition of a Watt in base metric units ($\frac{m^2 kg}{s^3}$).

$$\bar{P}_r = (V_a^3 \rho K_{p1} + \frac{W^2}{V_a \rho}\frac{\cos^2(\gamma)}{\cos^2(\phi)}K_{p2} + \frac{V_a W \sin(\gamma)}{\eta})(\frac{T^3}{L^2 M}) \tag{4.33}$$

There is no change in the scaled time state compared to the unscaled time state.

$$\dot{\bar{t}} = 1 \tag{4.34}$$

4.2.2 Results

The initial results using the constant gradient wind field are illustrated in the following set of figures. From these initial results, there are many different aspects that immediately jump out.

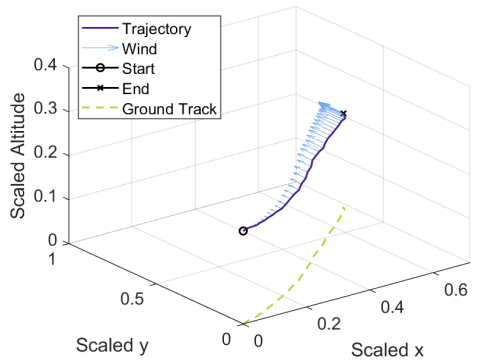

(a) Scaled Trajectory with Wind

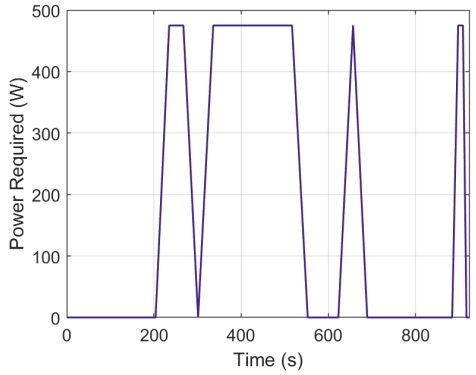

(b) Power Demanded

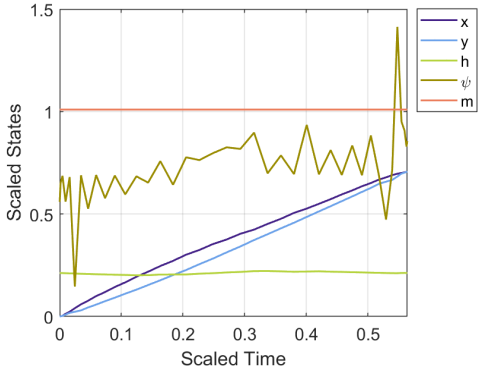

(c) Scaled State History

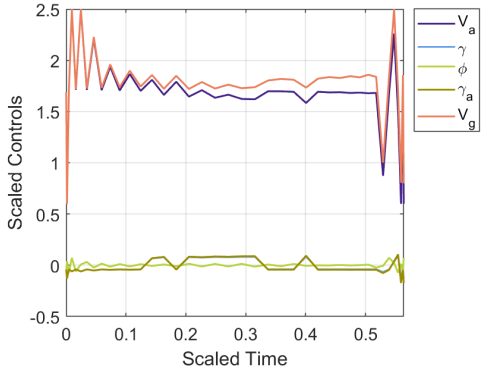

(d) Scaled Control History

Figure 4.1. Results: Initial DIDO Implementation

The problem was solved and the results are presented in Figure 4.1. With the wind field

having a constant gradient, intuition would expect smooth states and controls. However, Subfigure 4.1d shows oscillatory behavior in all control variables. Additionally, Subfigure 4.1c shows jittering in the heading angle, which is likely a result of oscillations in the bank angle, to which it is incredibly sensitive. Furthermore, Subfigure 4.1b shows a "bang-bang" behavior for the power required. Intuition would not suggest this. To get a deeper insight into possible issues with the numerical solution, it is helpful to examine the dual space results.

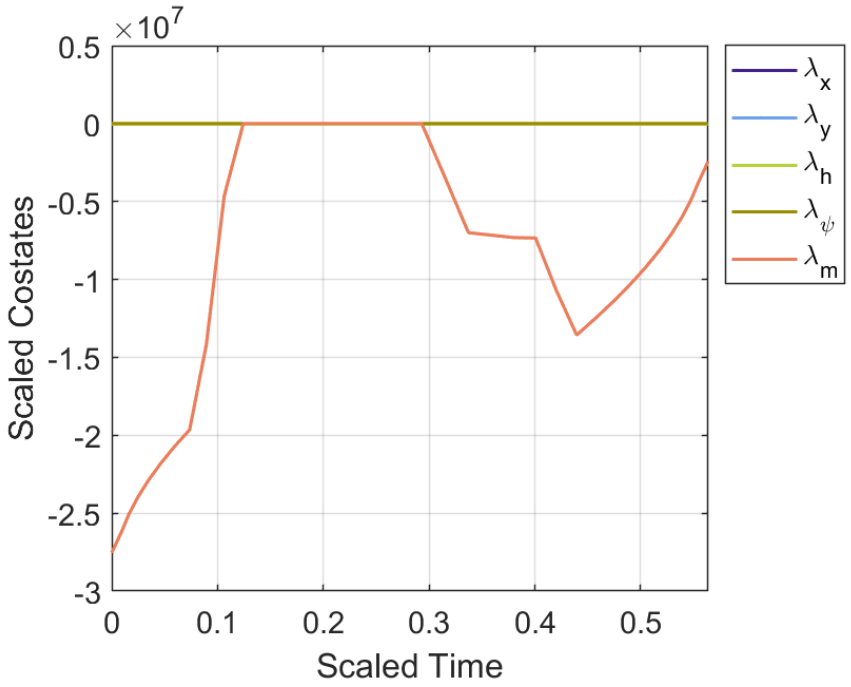

Figure 4.2. Scaled Costate History

From a quick glance at the costate history, shown in Figure 4.2, it is apparent that the mass costate is a potential source of numerical ill-conditioning. Being several orders of magnitude greater than its counterparts, even a tiny computational error in λ_m will balloon into a substantial error in other parts of the problem. Luckily, the cause of this issue is explainable and easily correctable.

4.3 Reformulation of Mass Scaling

While scaling off of the initial mass of the aircraft was a reasonable starting point, it is evident that modifications must be made. The problem arises from the difference in magnitude between the initial mass and the fuel burn rate. Recall that the Hybrid Tiger has an initial mass of 23.93 kg and burns $\approx 9\frac{g}{hr}$ of fuel. The mass dynamic can be written as

$$m(t) \approx 23.93 - \frac{0.009}{3600}t \quad (kg). \tag{4.35}$$

Compared to the mass of the aircraft, the rate of mass loss due to fuel burn rate is extremely small. Furthermore, recall that to scale this problem, both the mass and fuel burn rate were divided by the initial mass — further reducing the scale of $\dot{m}$, and ballooning the size of λ_m. To begin addressing this, the mass will no longer be directly treated as a state. Rather, the change in mass will be defined as the new state Δm. Where mass is used in parts of the model, like the power required, it is now implemented as

$$m = m_0 + \Delta m, \tag{4.36}$$

where

$$\Delta\dot{m} = f(V_a, \gamma, \phi, m). \tag{4.37}$$

This may not seem like a significant modification. However, this allows a new scaling factor to be introduced which scales Δm directly. A strength of this change is that Δm by definition initializes at zero. Thus, it can be scaled by

$$\bar{\Delta m} = \frac{\Delta m}{DM}. \tag{4.38}$$

In Equation (4.38), DM is an estimate of the fuel the aircraft will consume during the flight trajectory. In this iteration of the problem, the value of DM was established manually, but a reasonable value for DM could be automatically computed via the Breguet range equation.

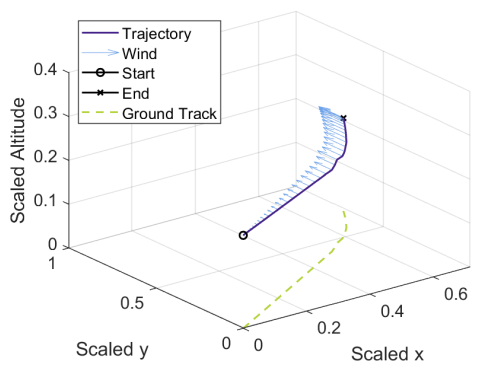

(a) Scaled Trajectory with Wind

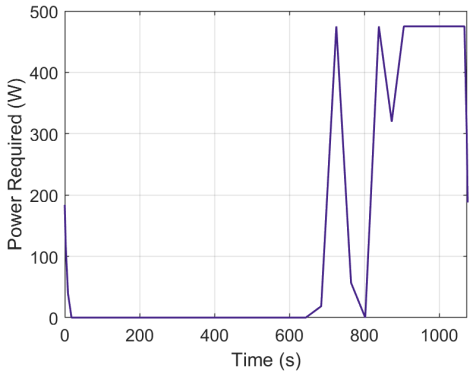

(b) Power Demanded

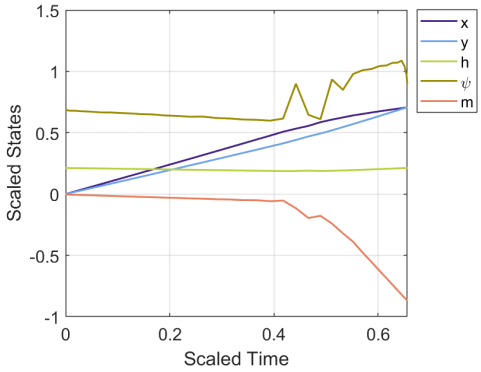

(c) Scaled State History

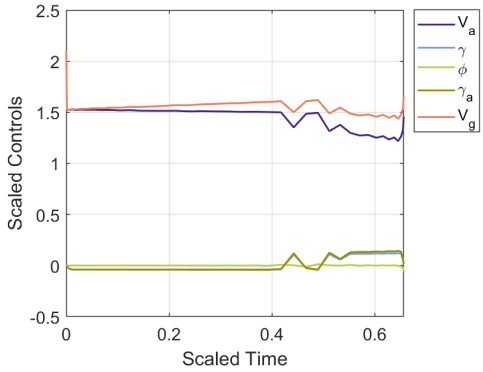

(d) Scaled Control History

Figure 4.3. Results: Refining Mass Scaling

The results shown in Figure 4.3 show an immediate improvement upon reworking the mass scaling. The unexpected fluctuations of the problem variables are reduced. However, this solution still has an unexpected behavior observed as the aircraft begins to turn more aggressively with the wind. Additional adjustments to the scaling are needed to further refine the solution.

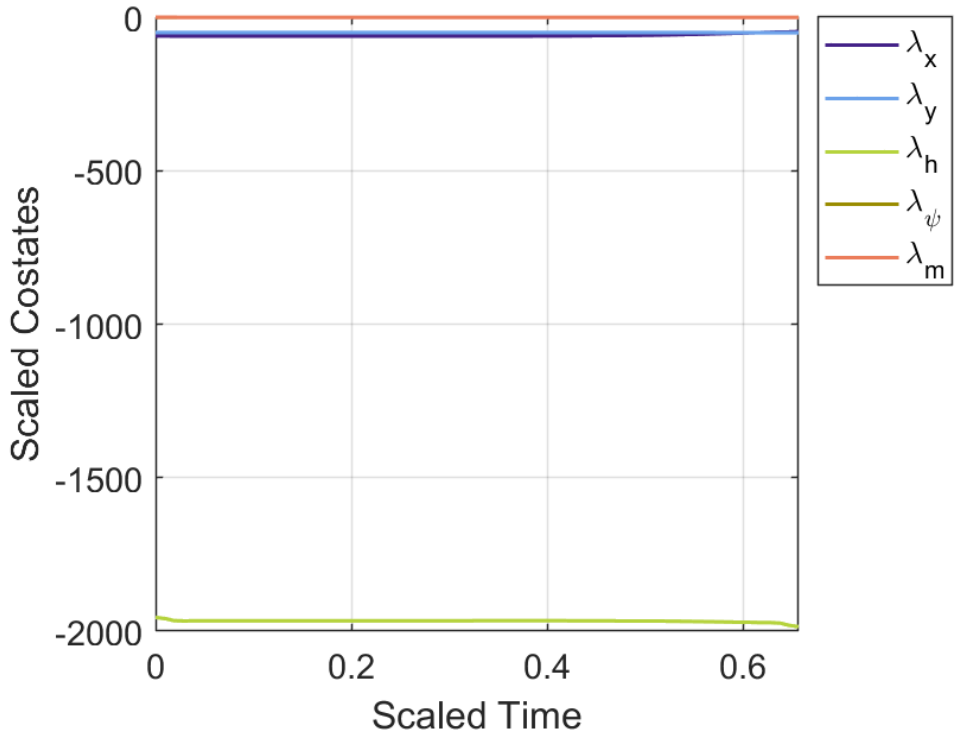

Figure 4.4. Scaled Costate History

Analyzing the dual space again provides two observations. First, the application of mass scaling has effectively corrected the scaling of the mass costate. From the definition of the mass costate given in Equation (3.15), since the fuel burn rate is so small, λ_m is expected to be nearly constant. This is now the case, as shown in Figure 4.4. The other notable finding from this plot is that now the altitude costate is a couple of orders of magnitude greater than the rest of the costates. By modifying the way distances are scaled, this too can be corrected.

4.4 Separation of Altitude Scaling

While a kilometer in altitude and a kilometer in ground track distance are the same, the variations of the distances and the altitudes are very different in a long-endurance flight. During a flight, aircraft can fly thousands of kilometers. However, the magnitude of the change in altitude for a flight is much smaller — ranging from no change in altitude, to at most a couple kilometers. Because of this, the ground track and altitude distances can and

should be separated and scaled appropriately. The Euclidean distance for the initial and final positions of the ground track is now used to scale x and y.

$$L = \sqrt{(x_f - x_0^2) + (y_f - y_0)^2} \tag{4.39}$$

The altitude is now scaled off the mean of the initial and final altitudes.

$$H_s = \frac{h_f + h_0}{2} \tag{4.40}$$

This results in the scaled altitude being around 1 during flight. However, be cautious in using this definition for H_s if the boundary values for altitude are low, and the aircraft is expected to have a substantial climb and descent during flight. That could result in the scaled altitude ballooning to a much greater magnitude compared to the other scaled states. An alternate scaling method that can be utilized in that scenario is to manually set the expected max altitude as H_s.

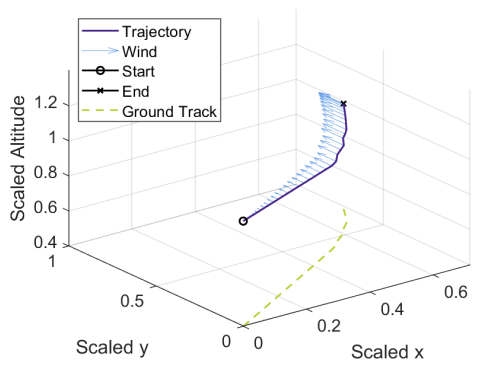

(a) Scaled Trajectory with Wind

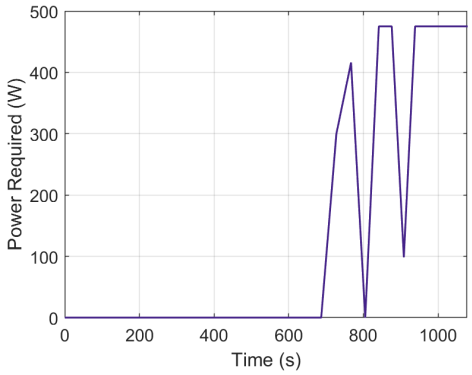

(b) Power Demanded

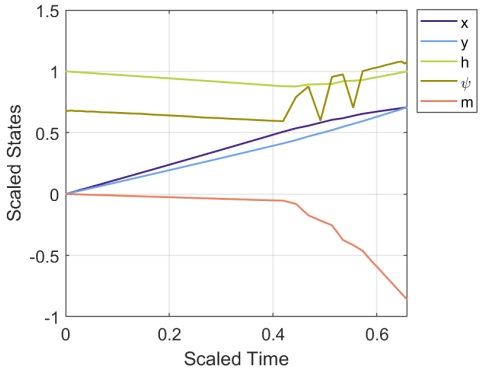

(c) Scaled State History

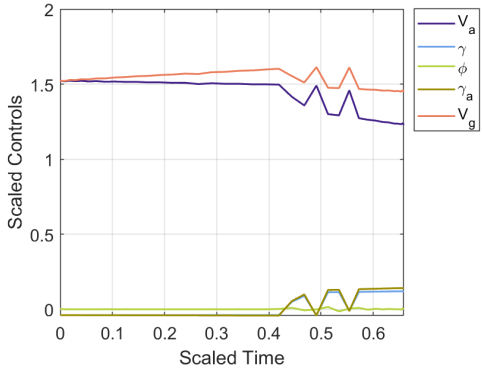

(d) Scaled Control History

Figure 4.5. Results: Refining Altitude Scaling

Scaling the altitude effected a small improvement in the results. The control history, shown in Subfigure 4.5d, no longer features the small oscillations that were observed previously. However, there are two instances in the control history displaying unexpected behavior. During the climb, the aircraft drops its climb angle, increases its velocity, and turns more into the wind. For a constant wind gradient, this is an unexpected result. To continue refining the problem, the effects of the new altitude scaling factor on the dual space is shown in Figure 4.6 and analyzed.

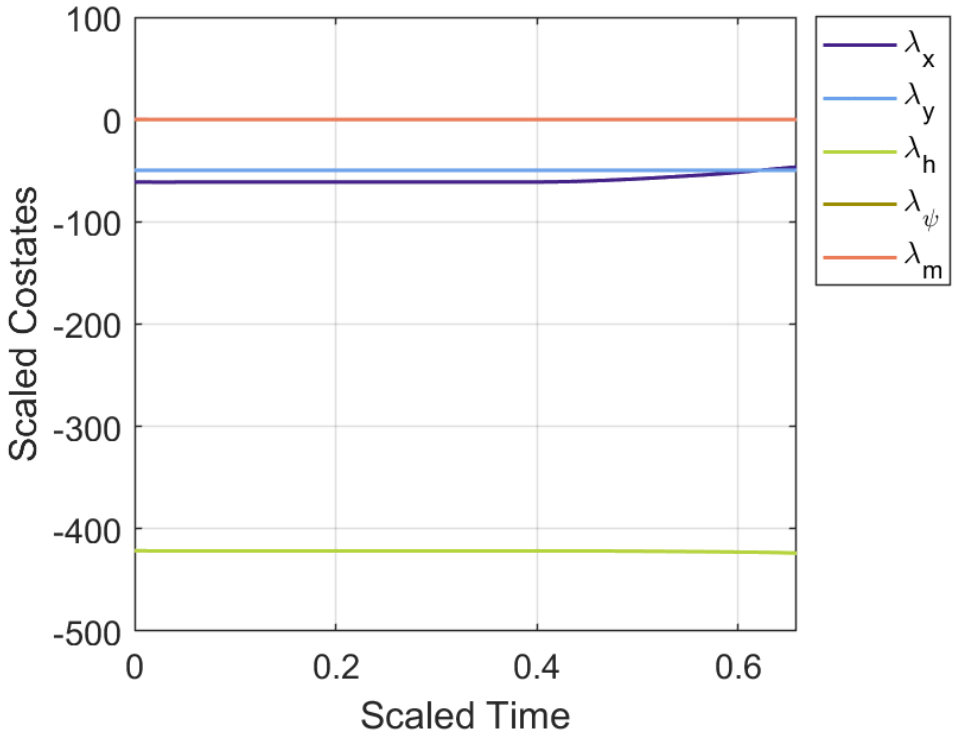

Figure 4.6. Scaled Costate History

Separately scaling the ground track and altitude did reduce the magnitude of the altitude costate. However, it still has the largest magnitude of any costate. Since air density is a function of altitude, and the density gradient in the atmosphere is relatively small, this is likely the cause. However, since the altitude is scaled to about 1, further modifications to its scaling will be avoided. With the states scaled, attention can be turned directly to the cost function.

4.5 Inclusion of a Mollifier

A mollifier is a smoothing function [12]. In the application here, the mollifier is a small constant multiplied by the square of control variables added to the cost function. This adds a small amount of "inertia" to the control variables. It acts as a damper by adding a very

small weight to penalize the activity of the control states. This is expressed as

$$J[X(\cdot), U(\cdot)] = \int_{t_0}^{t_f} (P_r + \varepsilon U^2) dt, \tag{4.41}$$

where

$$0 < \varepsilon << 1. \tag{4.42}$$

It was found that $\varepsilon = 0.0001$ was the smallest value that removed the fluctuations seen in previous results. The results with the mollifier added are shown in Figure 4.7.

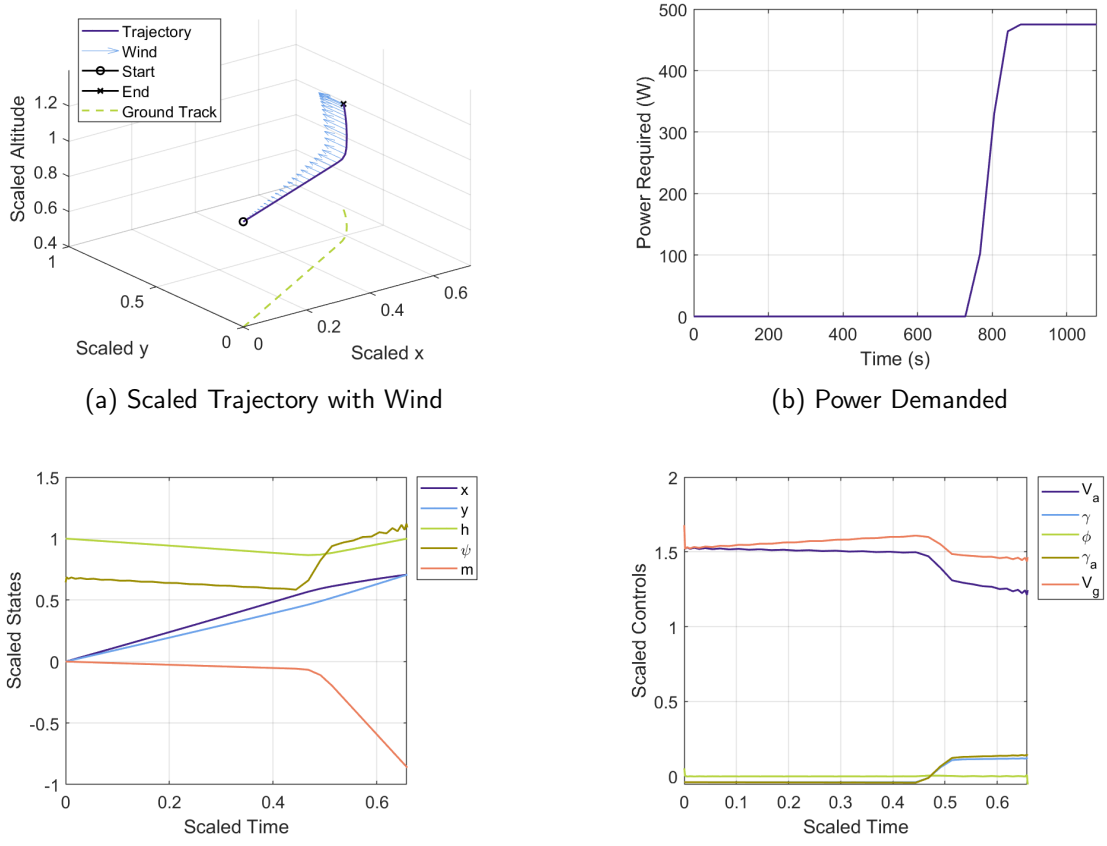

(a) Scaled Trajectory with Wind

(b) Power Demanded

(c) Scaled State History

(d) Scaled Control History

Figure 4.7. Results: Inclusion of a Mollifier

Along with the scaling process described, the inclusion of a mollifier appears to give the

expected results. The aircraft glides until favorable winds and then climbs to the final destination. However, more in-depth verification and validation of results is required. This is accomplished via a propagation test in Section 4.5.1 to demonstrate the feasibility and analysis of optimality conditions in Section 4.5.4

4.5.1 Feasibility Test

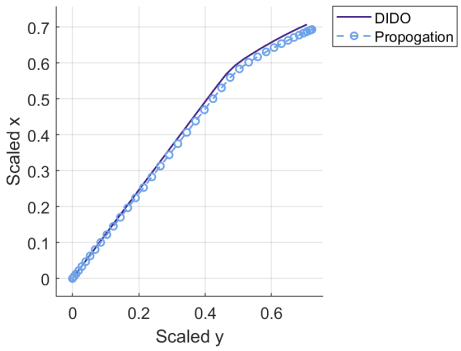

(a) Path

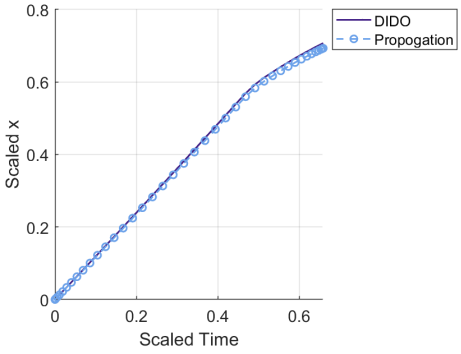

(b) State $\bar{x}$

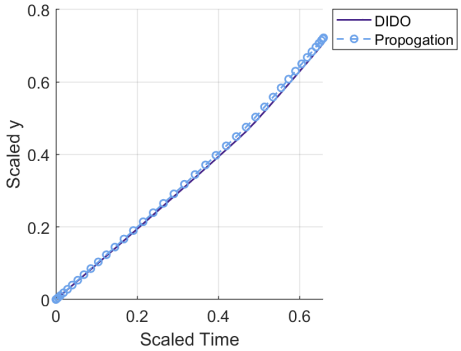

(c) State $\bar{y}$

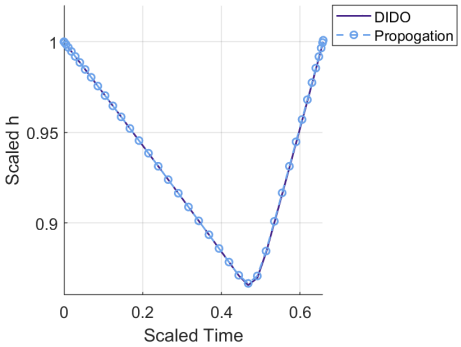

(d) State $\bar{h}$

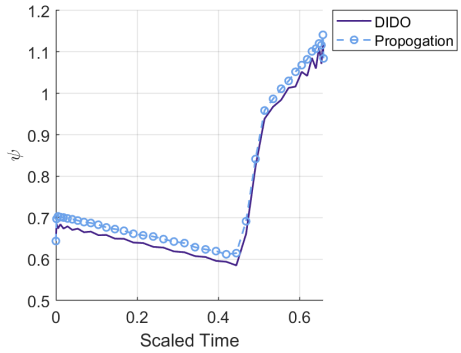

(e) State ψ

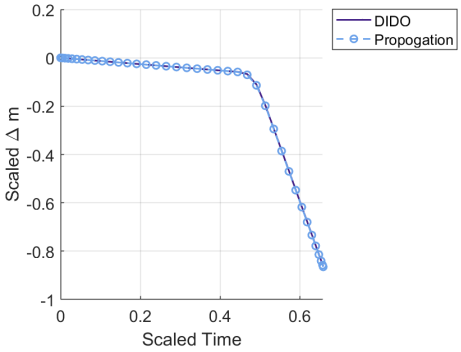

(f) State $\Delta\bar{m}$

Figure 4.8. Propagation Test of Path and State Variables

A propagation test is conducted to evaluate the ability of the system to match the expected state results when propagated forward in time. To accomplish this, the control history is propagated through the dynamics function in time via ODE45 and then compared to the results from DIDO. Overall, the results of the feasibility test closely tracks the DIDO solution. Subfigures 4.8a-4.8c show very slight errors in the ground track. These are a result of small heading errors, which can be observed in Figure 4.8e. This is due to the sensitivity of the heading error to small changes in the bank angle. However, these are minor and would be easily compensated for in flight by the aircraft's autopilot. Thus, the solution is feasible.

4.5.2 Refined Problem Formulation

Since the cost function has been altered to include a mollifier and the mass state has been modified, it is necessary to update the problem formulation developed in Chapter 2.

Minimize

$$J[X(\cdot), U(\cdot)] = \int_{t_0}^{t_f} \left(V_a^3 \rho K_{p1} + \frac{m^2 g^2}{V_a \rho} \frac{\cos^2(\gamma)}{\cos^2(\phi)} K_{p2} + \frac{V_a m g \sin(\gamma)}{\eta} + \varepsilon U^2 \right) dt,$$

on domain

$$X \in \mathbb{R}^6 \quad U \in \mathbb{R}^5 \,,$$

where

$$X = \begin{bmatrix} x \\ y \\ h \\ \psi \\ \Delta m \\ t \end{bmatrix} \qquad U = \begin{bmatrix} V_a \\ \gamma \\ \phi \\ V_g \\ \gamma_a \end{bmatrix}, \tag{4.43}$$

subject to

$$\dot{x} = V_a \cos(\psi) \cos(\gamma_a) + w_N, \tag{4.44}$$

$$\dot{y} = V_a \sin(\psi) \cos(\gamma_a) + w_E, \tag{4.45}$$

$$\dot{h} = V_a \sin(\gamma_a) - w_D, \tag{4.46}$$

$$\dot{\psi} = \frac{g}{V_a}\tan(\phi), \tag{4.47}$$

$$\Delta\dot{m} = f(V_a, \gamma, \phi, m), \tag{4.48}$$

$$\dot{t} = 1, \tag{4.49}$$

with boundary conditions

$$m(t_0) = m_0, \tag{4.50}$$

$$x(t_0) = x_0 \quad x(t_f) = x_f, \tag{4.51}$$

$$y(t_0) = y_0 \quad y(t_f) = y_f, \tag{4.52}$$

$$z(t_0) = z_0 \quad z(t_f) = z_f, \tag{4.53}$$

$$t(t_0) = 0, \tag{4.54}$$

and path constraints

$$h_1 := V_a^2 + V_w^2 - V_g^2 + 2V_a(\cos(\psi)\cos(\gamma_a)w_n + \sin(\psi)\cos(\gamma_a)w_e - \sin(\gamma_a)w_d) = 0, \tag{4.55}$$

$$h_2 := \frac{V_a \sin(\gamma_a)}{V_g} - \sin(\gamma) = 0, \tag{4.56}$$

$$h_3 := h_L \leq h \leq h_U, \tag{4.57}$$

$$h_4 := \Delta m_e \leq \Delta m, \tag{4.58}$$

$$h_5 := P_{min} \leq P_r \leq P_{max}. \tag{4.59}$$

4.5.3 Changes to the Necessary Conditions

Since the problem formulation has been updated, all of the equations developed in Chapter 3 must be updated before evaluating optimality. Luckily, most of the equations remain largely unaffected by the changes to the problem formulation. For the adjoint equations, the only change is in notation. Redefining m as $m_0 + \Delta m$ does not change the time behavior of the costates.

With a mollifier being added to the cost function, there is a slight change to all of the Hamiltonian minimization conditions. Each control variable's optimality condition now

has the addition of the partial derivative of the mollifier.

$$\frac{\partial}{\partial U}(\varepsilon U^2) = 2\varepsilon U \tag{4.60}$$

So for all minimization conditions in Section 3.3, with the changes made in this chapter, necessitate the addition of $2\varepsilon U$, where U is replaced by the appropriate control variable.

There are no changes to the boundary conditions, so the transversality condition remains unchanged. Finally, there are no changes to the time dependency of the problem. Therefore, neither the Hamiltonian Evolution Equation nor the Hamiltonian Value Condition requires modification.

4.5.4 Optimality Checks

A constant gradient wind field was selected to provide simple intuition on what the optimal solution should look like, however, this does not substitute performing optimality checks. To accomplish these checks, the equations developed in Chapter 3 and refined above in Section 4.5.3 are compared to aspects of the numerical solution.

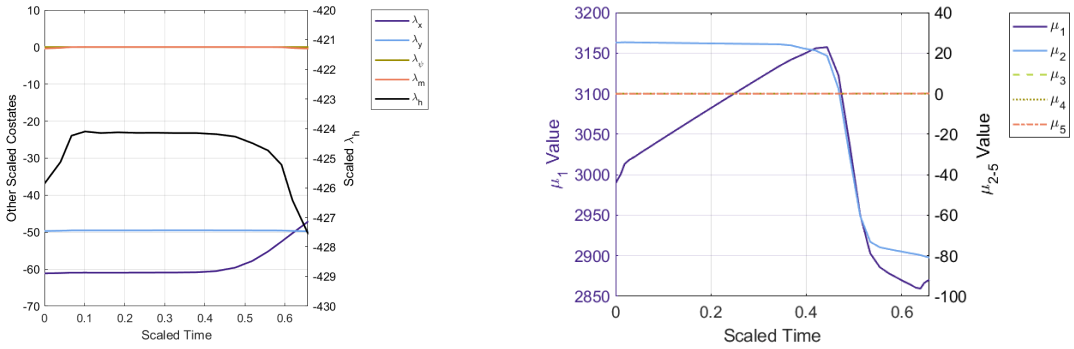

(a) Costate History (b) Complementary Condition

Figure 4.9. Necessary Conditions for Optimality Checks

The first part of this analysis verifies that the costate history, shown in Subfigure 4.9a, follows the adjoint equations and adheres to the transversality conditions. First, both ground

track states follow the adjoint equations.

$$\dot{\lambda_x} = -\lambda_x \frac{\partial w_N}{\partial x} - \lambda_y \frac{\partial w_E}{\partial x} + \lambda_h \frac{\partial w_D}{\partial x} = -\frac{3\lambda_y}{L} \tag{4.61}$$

With the wind blowing to the east, all other terms go to zero. Since the wind is scaled in terms of scaled x, $\bar{x}$, the scaling factor L appears in the result. This results in a very small increase in λ_x, which is observed in Sub-Figure 4.9a.

$$\dot{\lambda_y} = -\lambda_x \frac{\partial w_N}{\partial y} - \lambda_y \frac{\partial w_E}{\partial y} + \lambda_h \frac{\partial w_D}{\partial y} = 0 \tag{4.62}$$

The wind does not vary with y, so λ_y is constant. This aligns with the resulting costate history.

$$\dot{\lambda_h} = -\frac{\partial P_r}{\partial h} - \lambda_x \frac{\partial w_N}{\partial y} - \lambda_y \frac{\partial w_E}{\partial y} + \lambda_h \frac{\partial w_D}{\partial y} - \lambda_m \frac{\partial \dot{m}}{\partial h} - \mu_3 - \mu_5 \frac{\partial P_r}{\partial h} \approx 0 \tag{4.63}$$

Moving onto the remaining position costate, the altitude costate is consistent with expectations. The wind does not vary with altitude, so all wind-dependant terms are zero. The derivative of the altitude on power and fuel burn is small enough to be approximated as zero. This can be shown by taking the partial derivative of the density model with respect to the altitude.

$$\frac{\partial \rho}{\partial h} = -0.0001 e^{\frac{-h}{10400}} \tag{4.64}$$

Finally, Subfigure 4.9b shows that μ_3 and μ_5 are zero. Consistent with this, λ_h is constant in the costate history.

$$\dot{\lambda_m} = -\frac{\partial P_r}{\partial m} - \lambda_m \frac{\partial \dot{m}}{\partial m} - \mu_4 - \mu_5 \frac{\partial P_r}{\partial m} \approx 0 \tag{4.65}$$

For the same reasons as above, the fuel-burn costate is approximated as zero. Additionally, Subfigure 4.9b shows that μ_4 is also zero. Thus, Equation (4.65) is consistent with the results in Subfigure 4.9a.

$$\dot{\lambda_\psi} = \lambda_x V_a \sin(\psi)\cos(\gamma_a) - \lambda_y V_a \cos(\psi)\cos(\gamma_a) \approx 0 \tag{4.66}$$

Unlike the other costates, the heading angle costate dynamics were harder to draw direct

conclusions from. However, numerically evaluating Equation 4.66 shows that in this case, λ_ψ shall be zero, which is consistent with Subfigure 4.9a. Next, the transversality conditions are analyzed.

$$\lambda_\psi(t_f) = \frac{\partial \bar{E}}{\partial \psi_f} = 0 \tag{4.67}$$

$$\lambda_m(t_f) = \frac{\partial \bar{E}}{\partial m_f} = 0 \tag{4.68}$$

Only the mass and heading angle costates have a known final boundary condition — both being zero at the final time. This matches the costate history.

Next, the Hamiltonian is analyzed for optimality by checking the Hamiltonian Evolution Equation and Hamiltonian Value Condition against the result shown in Figure 4.10.

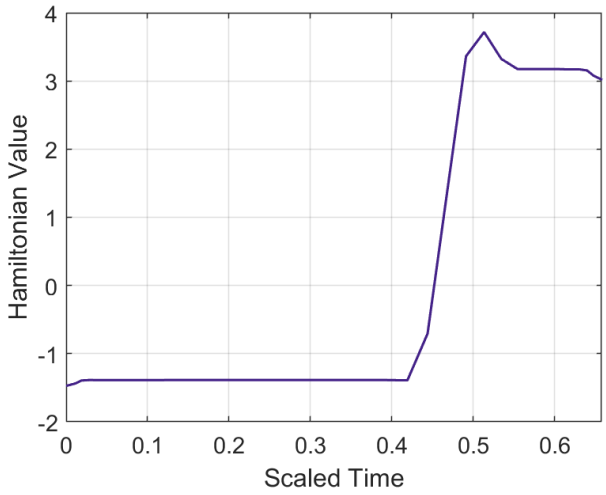

Figure 4.10. Hamiltonian Evolution

From the Hamiltonian Evolution Equation, the expected behavior is that the Hamiltonian shall be constant in time. From the Hamiltonian Value Condition, it is known that the value at the final time shall be zero. Combining those, the expectation is that the Hamiltonian shall be zero for all time. Looking at Figure 4.10 it could be surmised that this is not the case. However, this is a product of the scale of the problem. Considering the high value of costates and constraints, this is within an acceptable error of numerical zero. Scaling of the path functions is one way to correct this.

4.6 Chapter Summary

This chapter demonstrates the implementation of the energy-optimal problem statement in DIDO and the verification and validation of the solution. It begins by defining the problem and develops a method of scaling the problem statement before its implementation. This chapter then shows the iterative process of analyzing the initial results and incorporating changes to improve the numerical solution. Through refining the problem statement by modifying multiple scaling factors, reformulating the mass state, and adding a mollifier to the cost function, a viable candidate solution is achieved. To verify and validate this solution, a feasibility test and optimality checks are conducted. Now, with this refined problem statement, additional cases are solved and discussed in Chapter 5.

THIS PAGE INTENTIONALLY LEFT BLANK

CHAPTER 5:
Minimum Energy Planning Results

This chapter highlights the flexibility of the optimal control problem statement by documenting three unique and practically important scenarios. To especially highlight the incorporation of altitude into the model, the first two cases discuss scenarios that could not be previously evaluated with a 2-D energy optimal trajectory solver. The first features boundary conditions which require the aircraft to climb in the presence of varying vertical wind magnitudes. To draw further insight, additional runs are completed which vary the final altitude boundary condition. The next case makes use of the altitude constraint, utilizing it to generate an obstacle that the aircraft must avoid. The available climb rate of the aircraft is then varied to analyze the differences in the resulting trajectories. Finally, a case with a wind magnitude that decays with time is presented. All cases are run using the parameters and constraints from Hybrid Tiger. Like in Section 4.5.4, all cases were evaluated for optimality and were determined to meet the optimality conditions satisfactorily. However, for brevity, the optimality plots have been omitted.

5.1 Updraft

The first trajectory in this section combines two of the new capabilities gained by incorporating altitude into the model by demonstrating position-varying vertical wind and boundary conditions that require the aircraft to climb to the final position. Combing both of these allows for an interesting test case. By defining the wind such that there is none on a straight-line climb path, but then gradually increases further away, it can be observed how far the energy-optimal trajectory deviates from the direct route. To begin, the aircraft boundary conditions are defined for the aircraft to fly 10 km North and climb to 2 km from its initial

altitude of 1 km. The problem is not time-bounded.

$$(t_0) = (0) \quad (s) \tag{5.1}$$
$$(x_0, x_f) = (0, 10) \quad (km) \tag{5.2}$$
$$(y_0, y_f) = (0, 0) \quad (km) \tag{5.3}$$
$$(h_0, h_f) = (1, 2) \quad (km) \tag{5.4}$$

The vertical wind is defined as a parabola with varying strength in y. There is no lateral wind velocity. The constants defining the parabola were chosen such that at $y = 0, w_d = 0$ and gradually increase to $w_d = -2$ at $y = 2000$.

$$w_d = \frac{2}{2000^2}(y - 2000)^2 - 2 \quad (\frac{m}{s}) \tag{5.5}$$

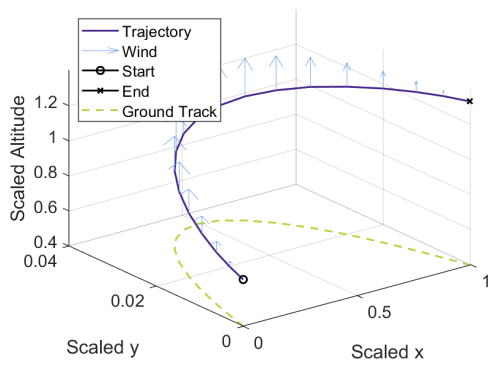

(a) Scaled Trajectory with Wind

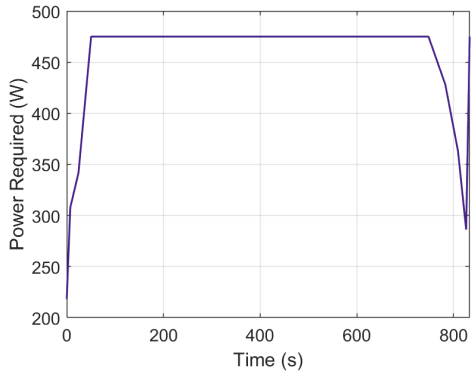

(b) Power Demanded

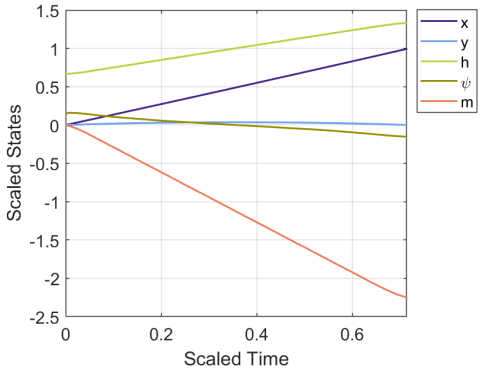

(c) Scaled State History

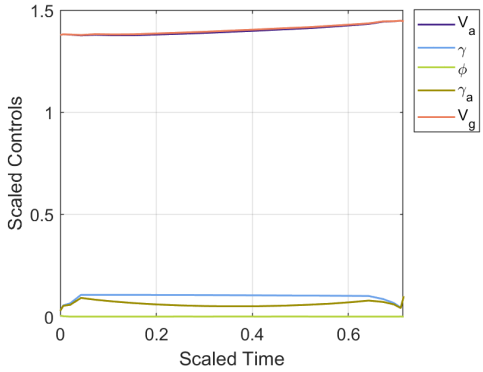

(d) Scaled Control History

Figure 5.1. Results: Updraft Case

Subfigure 5.1a shows that in this trajectory, the aircraft deviated from the straight line path by about 300 m. Subfigure 5.1b shows that the aircraft is flying at max power for almost the entire trajectory. Therefore, it is unclear whether the aircraft is deviating from the straight line to capture more of the beneficial updraft effects or if the climb required is too great to complete in the 10 km distance between boundary conditions. To gain more insight into what is happening in this result, in Subsection 5.1.1, the final altitude boundary condition is varied across runs.

It should be noted that the solution was incredibly sensitive to the span of the search space for y. Since both the initial and final position of y are equal, the distance covered in y is much

smaller than x, this problem was not well scaled. However, a very similar change to the one shown in Section 4.4 could be implemented in the future to avoid this problem. Just like altitude is separately scaled from the x and y, so too could the scaling of the lateral position states be separated. However, since DIDO was able to converge to an optimal solution, this change was not implemented in this work.

5.1.1 Varying Final Altitude

To further analyze the updraft case, the solution was run five times with the final altitude varying from 1500 m to 2500 m.

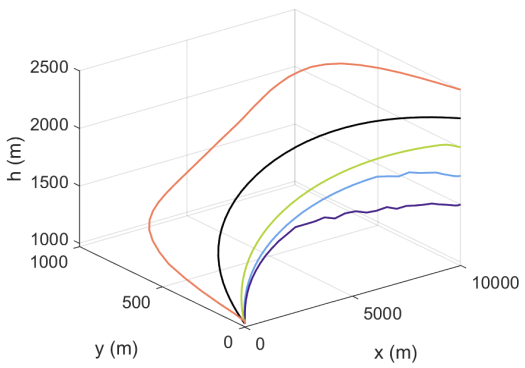

(a) Resulting Trajectories

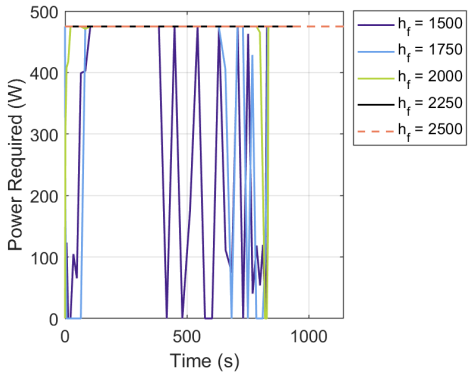

(b) Power Demanded

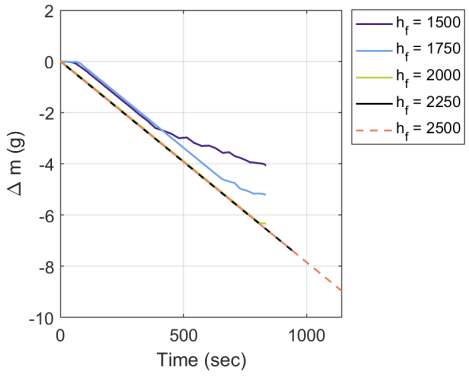

(c) Fuel Consumption

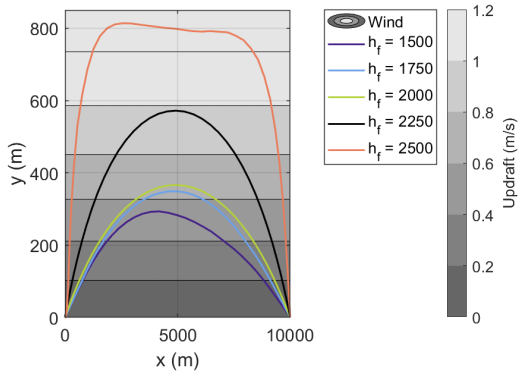

(d) Ground Track overlaid to Wind

Figure 5.2. Results: Varying Final Altitude

Subfigures 5.2a and 5.2d show the trajectory of the five runs, with the aircraft deviating from the straight line path increasingly as the prescribed final altitude increases. Though these mostly provide context as the answer to whether the aircraft is primarily deviating to capture the updraft or because it is limited by the available climb rate is found in Subfigures 5.2b and 5.2c. Subfigure 5.2b shows the power required over time, but is an incredibly noisy graph. This could imply that the solution is not particularly sensitive to the exact value of power required. This could also be a product of the Hybrid Tiger having a small maximum power. However, instead of trying to parse the power subfigure, the same information is more clearly conveyed by looking at the fuel burn over time shown in Subfigure 5.2c. Surprisingly, starting from the lowest altitude final position, the first three runs all culminate within 2 seconds of each other and do not maintain the max fuel burn rate across the trajectory (though the 2000 m comes very close). Unlike those cases, the two higher final altitude cases maintain the maximum fuel rate for the entire trajectory. This difference can be used to gain insight into what is the primary factor driving the aircraft to deviate from the straight-line trajectory. For the first two cases, the trajectory is primarily deviating to capture the energy benefit from the updraft. For the last two cases, the aircraft is primarily deviating because of limitations in the available climb rate, while still utilizing the updraft. Coincidentally, the original run with the final altitude of 2000 m just happened to be right at the dividing line between these two behaviors.

5.2 Terrain Avoidance

This section demonstrates how, by modifying the altitude constraint's lower bound to be a surface, terrain avoidance can be incorporated into the model. For this case the drone is to fly from the origin to 10 km East, beginning and ending at an altitude of 3 km. The final time is unbounded.

$$(t_0) = (0) \quad (s) \tag{5.6}$$

$$(x_0, x_f) = (0, 0) \quad (km) \tag{5.7}$$

$$(y_0, y_f) = (0, 10) \quad (km) \tag{5.8}$$

$$(h_0, h_f) = (3, 3) \quad (km) \tag{5.9}$$

The particular construction of the lower constraint for this case has been modeled through a combination of trigonometric waves to create an obstacle between the initial and final position. This has been chosen such that the obstacle would significantly impede the path of the aircraft, allowing for additional analysis of the resulting trajectory. In a less extreme case, this same principle could be used to model a mountain plus a minimum altitude that must be kept above it. The altitude constraint is updated to reflect the new lower altitude bound.

$$h_3(x) := 3000(\sin(\frac{y-2000}{2000}) + \cos(\frac{x}{2000})) \leq h \leq 15000 \quad m \tag{5.10}$$

To explicitly highlight the interactions between the constraint and the trajectory, no wind is present in this run.

$$w = [0,0,0]^T \quad (\frac{m}{s}) \tag{5.11}$$

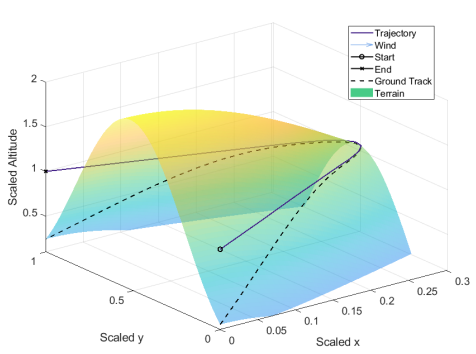

(a) Scaled Trajectory

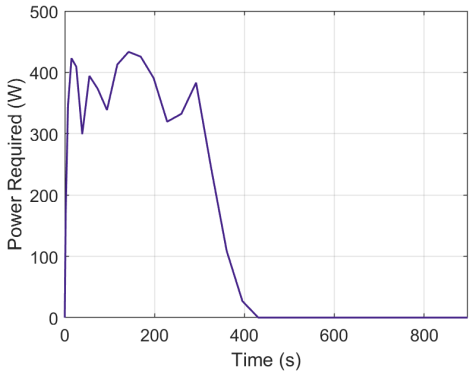

(b) Power Demanded

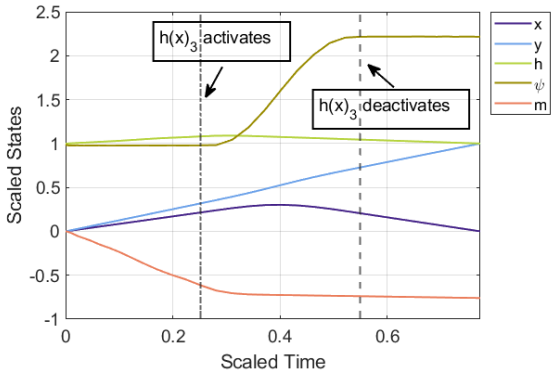

(c) Scaled State History

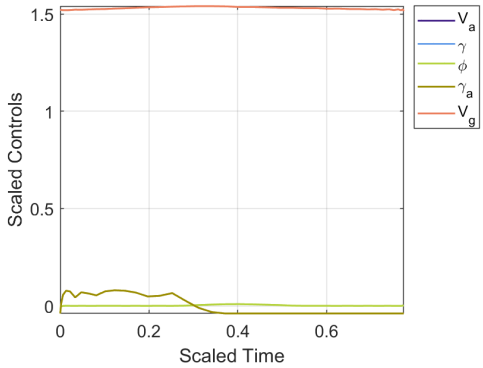

(d) Scaled Control History

Figure 5.3. Results: Terrain Avoidance Case

Subfigure 5.3a shows the aircraft's trajectory and ground path overlaid onto the constraining surface. The trajectory shows an initial climb, primarily flying laterally to get around the obstacle, and then a glide into the final position. Subfigure 5.3b shows the power required to fly this trajectory. It should be noted that the optimal trajectory did not need to utilize the full power of the Hybrid Tiger at any point in the trajectory. The initial climb was not a maximum power climb, suggesting the energy-optimal trajectory calls for this particular obstacle to be avoided primarily by going around rather than over it. Finally, the control history in Subfigure 5.3c shows the state history with the constraint activation times overlaid. When the constraint is active, the aircraft's trajectory is equal to the lower-bounded surface. Rather than any radical change occurring when the trajectory encounters the constraint, the

trajectory meets the surface at a tangent and gently follows it around until it has cleared the obstacle.

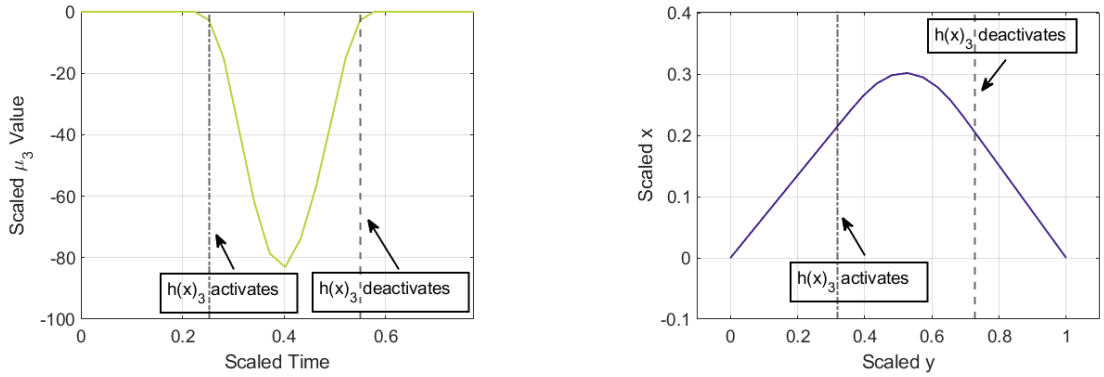

(a) Complementary Condition (b) Scaled Path

Figure 5.4. Altitude Constraint's Activation

Figure 5.4 provides additional context to the activity of the constraint. Subfigure 5.4a shows μ_3 departing zero, which signifies activation, during the middle of the trajectory. By only looking at the ground path, shown in Subfigure 5.4b, it would not be apparent where the trajectory was against the constraining surface. However, with the information from μ_3 overlaid, it becomes clear that the aircraft flies a trajectory tangent to the surface, and then departs the surface on a tangent glide slope to the final position.

5.2.1 Varying Available Climb Rate

To further analyze the optimal trajectory around the obstacle, three cases with differing available climb rates were run. To modify the available climb rate, Hybrid Tiger's initial weight was varied from 20.9 kg to 25.9 kg without modifying any other parameters. A primary interest of this investigation was to see whether giving the aircraft a higher available climb rate would cause it to crest the hill at a higher point closer to the boundary conditions.

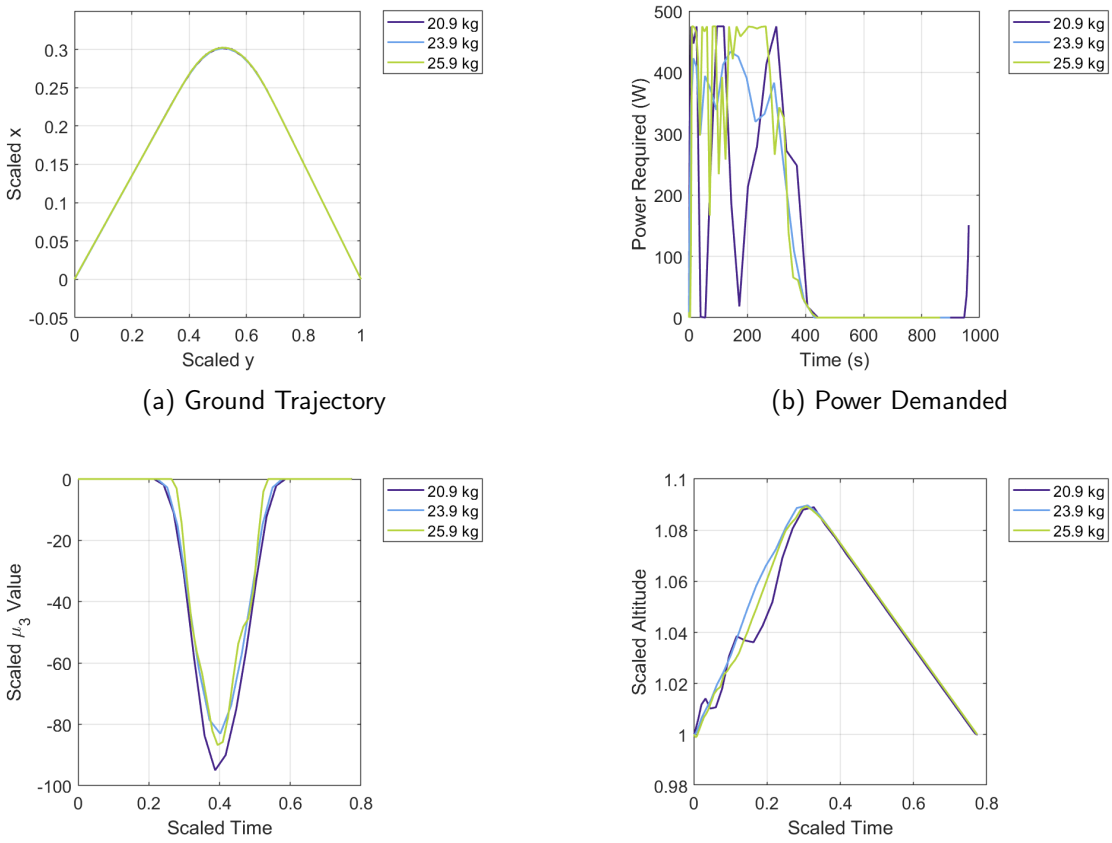

(a) Ground Trajectory

(b) Power Demanded

(c) Complementary Condition

(d) Scaled Control History

Figure 5.5. Terrain Avoidance: Climb Rate Comparison

Subfigure 5.5a shows a comparison of the scaled ground track and Subfigure 5.5d shows a comparison of the scaled altitudes over time. Surprisingly, the available climb rate did not affect the path taken by the aircraft. The ground track is the same for each case. There are some slight differences and fluctuations in the altitude, but those seem to be introduced by slight errors and not from differing trajectories. Subfigure 5.5b shows that for all cases the initial climb uses the top of its power range. However, as in the case of the updraft case, this plot does not serve particularly well for comparison. To compare, it easily to quantify the trajectories based on the time integral of power — the total energy required.

Table 5.1. Comparison of Energy Required

Weight (kg)	Energy Required (kJ)
20.9	124.6
23.9	130.7
25.9	134.4

Following expectations, the energy required increases with the weight of the aircraft, even with the fluctuations observed in the climb of the lightest aircraft.

5.3 Time-Varying Wind

The final case highlights the ability to converge to a numerical solution when the wind varies with time. Since weather patterns are always changing, this shows the system's capability to effectively navigate through fluctuating atmospheric conditions. For this case, the wind is defined as

$$w = [\frac{a}{t+b}, 0, 0]^T \quad (\frac{m}{s}), \tag{5.12}$$

with constants

$$a = 800 \qquad b = 800. \tag{5.13}$$

These constants have been selected to give a 1 $\frac{m}{s}$ southerly wind at initialization, which decays to about half its magnitude at the estimated final time.

$$(t_0) = (0) \quad (s) \tag{5.14}$$

$$(x_0, x_f) = (0, 0) \quad (km) \tag{5.15}$$

$$(y_0, y_f) = (10, 10) \quad (km) \tag{5.16}$$

$$(h_0, h_f) = (2, 2) \quad (km) \tag{5.17}$$

The boundary conditions are defined such that the aircraft begins at the origin and must arrive at 10 kilometers in both the North and East directions. There is no specified time at which it must arrive at this point. Finally, the flight path begins and must end at an altitude of 2 kilometers.

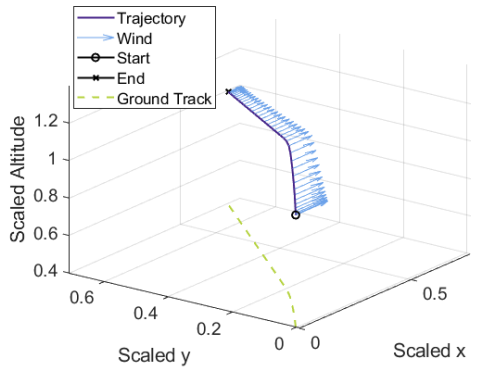

(a) Scaled Trajectory with Wind

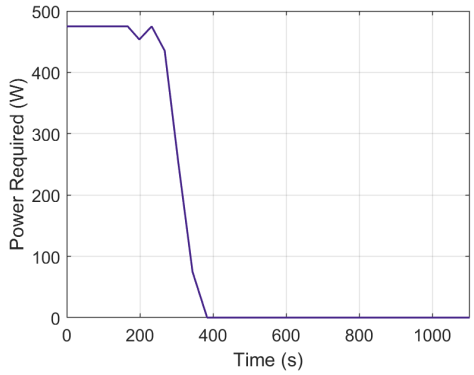

(b) Power Demanded

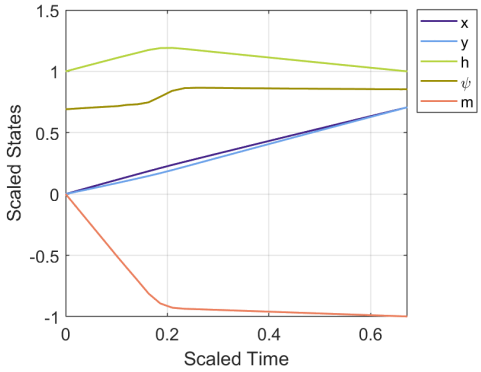

(c) Scaled State History

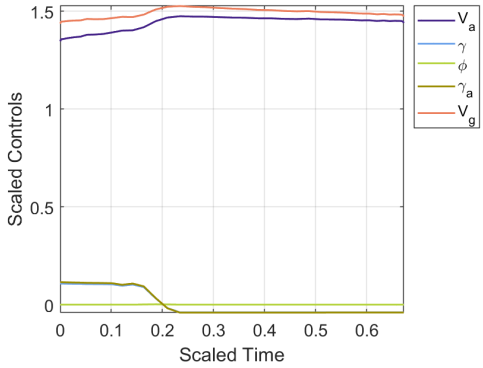

(d) Scaled Control History

Figure 5.6. Results: Time-Varying Wind Case

The results of the time-varying wind case are shown in Figure 5.6. These results share many similarities with the case discussed in Chapter 4. Recall that in that case, the aircraft maintained a glide slope until it reached the more favorable winds. The aircraft then climbed to the final position. In this case, the most favorable winds are at the initial time. Here, the aircraft initially climbs and then glides to the final position as the winds begin to die down. In both cases, the aircraft climbs in the presence of more favorable winds. This case also gives another opportunity to discuss the Hamiltonian, as this is the only case contained in this thesis where the expected Hamiltonian Evolution is not a constant zero.

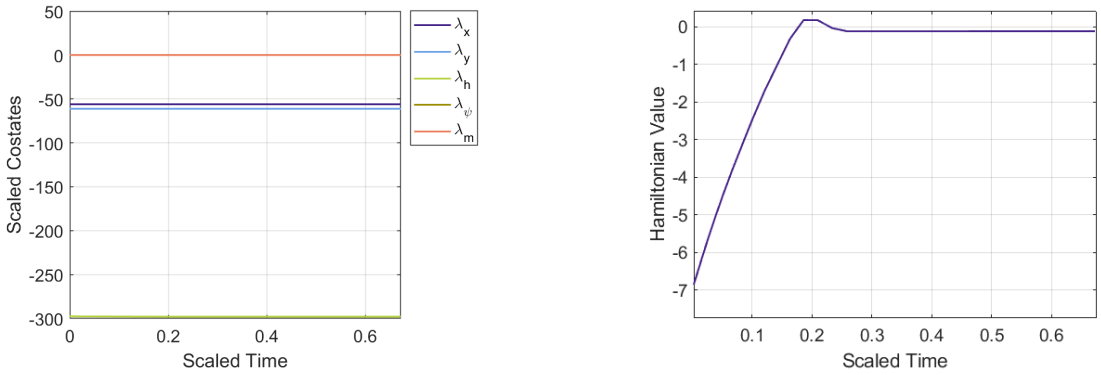

(a) Costate History

(b) Hamiltonian Evolution

Figure 5.7. Plots Required to Validate Hamiltonian Evolution

Figure 5.7 shows the costate history and the Hamiltonian Evolution. With a time-varying wind, the expected Hamiltonian evolution is dependent on the position costates and the time derivative of the wind.

$$\frac{\partial \bar{H}}{\partial t} = \frac{d\bar{\mathcal{H}}}{dt} = \lambda_x \frac{\partial w_N}{\partial t} + \lambda_y \frac{\partial w_E}{\partial t} - \lambda_h \frac{\partial w_D}{\partial t} = -\lambda_x \frac{a}{(t+b)^2} \tag{5.18}$$

From Equation (5.18), it is expected that the Hamiltonian has a positive slope whose magnitude decreases over time. The Hamiltonian Value Condition remains unchanged, so the expected final value of the Hamiltonian is zero. Subfigure 5.7b is within an acceptable range of this behavior, but shows that the solution can be improved. An improved solution would display the Hamiltonian beginning at a negative value, increasing over time, and gently tapering off to a final value of zero.

5.4 Chapter Summary

This chapter showcases how the energy-optimal problem formulation can be applied in many unique ways. Three cases, which all highlight key aspects of this thesis, were selected. An updraft, various commanded climbs, and terrain avoidance all showcase different elements that the inclusion of altitude into the model allows. The chapter concludes by showing a time-varying wind case and discusses the resulting time-dependent Hamiltonian. In the next

chapter, the results are summarized and some conclusions are drawn.

THIS PAGE INTENTIONALLY LEFT BLANK

CHAPTER 6:
Conclusion

This thesis developed and solved a trajectory optimization problem for finding the energy-optimal trajectory through a 3-Dimensional, time-varying wind field. Building on previous work, the incorporation of altitude and changes in weight had to be considered. This started by constructing a model of the system and formulating it into an optimal control problem statement. From there, Pontryagin's principle provided the needed conditions for transforming the problem statement into a boundary value problem and providing the conditions for optimality. After initial implementation in DIDO, continued iterations on scaling and problem formulation refined the numerical implementation. Multiple test cases were evaluated further to demonstrate the flexibility of the optimal control problem statement, with all solutions passing verification and validation checks.

This work contributes to efforts to increase the energy efficiency of our nation's military aircraft. Energy efficiency has a tangible tactical application by increasing our air assets' time-on-station, operational range, payload capacity, and other performance metrics. Since performance gains from energy efficiency are compounding, ultra-high endurance ISR UAS are innately the most suitable application for this research. This thesis serves to establish the underlying method and provide a proof of concept implementation. However, there are still many steps that will need to be taken in order to transition this work into operational software. As UAS continues to significantly push the envelope on maximum flight endurance, utilizing energy-aware guidance software will further compound their exceptional performance.

6.1 Future Work

The proceeding chapters have laid the foundation for a 3-Dimensional energy-aware guidance system. In order to transition this to an operational system, there are several areas that must be developed. This includes the introduction of real-world data, potential test cases to run with the inclusion of that data and additional useful features. By addressing these sections, this work will evolve to be able to create practical flight plans.

6.1.1 Real-World Weather Data

One of the next immediate steps will be to transition from using a theoretical density model with the simulated wind to empirical data. This will require pre-processing and a verification process to implement. The weather data must be interpolated across the search space and the interpolating algorithm must result in the data having a continuous derivative, ruling out linear interpolation. This is because the costate dynamics are dependent on the derivatives of the weather data. If the solver comes across the discontinuity in the derivative, it will likely not be able to obtain a solution. Additionally, the selected interpolation algorithm must be able to be bench-marked for accuracy. As seen in the results of this thesis, very small changes in the wind can have significant impacts on the resultant trajectory. Here, the old adage of "garbage in, garbage out" applies. Without proper verification of the interpolation, the resulting trajectory can't be properly validated.

6.1.2 Real-World Terrain Avoidance

Section 5.2 showed that by utilizing the altitude constraint, terrain avoidance can be included in this guidance model. By defining the lower bound of $h_3(x)$ as a function of ground position, the aircraft successfully navigated around a surface, representing a mountain. The natural progression of this particular work is to implement real-world data terrain data. This comes with many of the same data processing issues that are discussed in Section 6.1.1. A possible source for this data could be the Shuttle Radar Topography Mission dataset [15].

6.1.3 Defining Flight Envelope with Path Constraints

For this thesis, no cases where the UAS would be near a stall were considered. Thus, it was sufficient to define the upper altitude as a fixed value, knowing it would not be flying near said value. However, it would be possible to utilize the upper bound of the altitude constraint, $h_3(x)$, as a stall constraint. With the power available constraint, $h_5(x)$, modeling the power-limited portion of the flight envelope, adding the stall constraint would complete the flight envelope — assuming no structural limitations. However, if there are structural concerns, a whole new path constraint based on dynamic pressure could be incorporated into the model.

6.1.4 Multi-Objective Missions

An interesting capability that could be explored is creating a system that is tasked with various objectives, without a set order, and letting the system automatically determine the complete energy-optimal trajectory. For example, take a mission profile where a UAS is tasked with taking aerial imagery of a set amount of targets before proceeding to a fixed point for continuous coverage. To maximize the fuel which the UAS has for time on station at that final point, it must find the most fuel-efficient route that includes all the set targets.

A method to accomplish this could start by structuring the targets as nodes in a graph network. Then Dijkstra's algorithm could be used, with the edges of the graph being energy required to travel between targets. The energy required would be calculated in the same manner as shown in this thesis. This would result in the trajectory which accomplishes all mission objectives in the most energy-optimal manner.

6.1.5 Full-Scale Flight

The results in this thesis demonstrated short segments of a flight, ranging from about 10 to 15 km of ground track, generally totaling about 20 minutes. Through different runs, it was found that setting nodes at 40 worked for all solutions. The elapsed time between nodes was about 30 seconds. Lower node counts would sometimes result in the solution not utilizing the wind as well as it potentially could. Higher node counts gave more opportunities for unwanted fluctuations in the control history to appear. With DIDO only allowing a max of 200 nodes, this presents a challenge in extending this particular implementation to generate full-scale trajectories. To accomplish this, further improvements to scaling, segmented trajectories, or utilizing another solver may be required.

6.1.6 Comparison to Historic Data

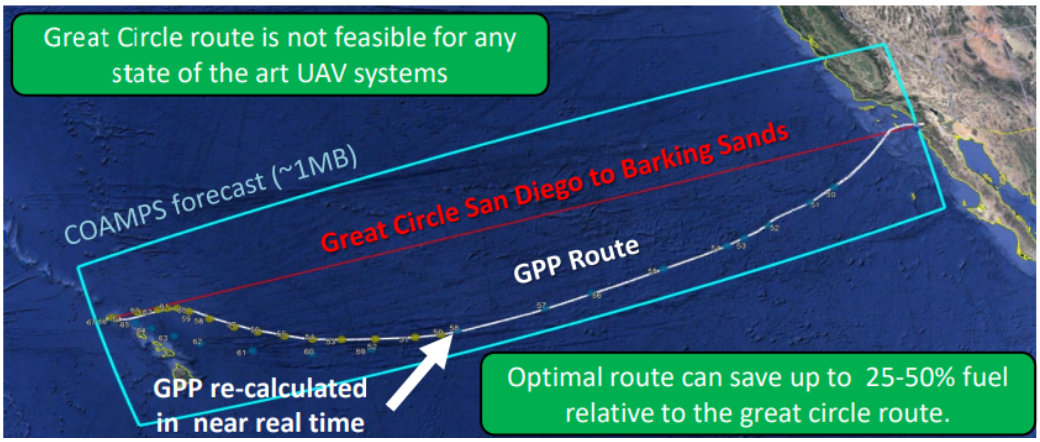

Figure 6.1. Hybrid Tiger flight from San Diego to Hawaii [16]

Once empirical weather data has been incorporated and the code is capable of solving full-scale flights, an important benchmark is comparing the data to previous flights to quantify the improvement. For example, Figure 6.1 is taken from previous work [16] on Hybrid Tiger, and shows the calculated energy optimal trajectory compared to a great circle route. This trajectory did not consider changes in altitude. Thus, this comparison would allow the improvement from a 2-D solution to a 3-D solution to be quantified.

6.1.7 Uncertainty

Using simulated atmospheric data allows for validating the model, expanding its functionalities, and simulating interesting cases. Using historic weather data serves can be used to show the expanded operational capabilities of particular aircraft and is one way to directly compare guidance systems to each other. However, those cases use definitive atmospheric data. In operational use, the system will be working with predictions from weather models — data that is anything but certain. By incorporating uncertainty into the weather data, the guidance system will become more robust and be more equipped to handle making adjustments if they are needed. By exploring things like probabilistic models and ensemble forecasting techniques, the optimization model will be able to more effectively account for the inherent uncertainty of predicted weather models. This will be a crucial step to enhance the reliability and resiliency of the system in practical operational scenarios.

APPENDIX:

A.1 P_R Derivation

This derivation opens with the equation for the translational dynamics of an aircraft.

$$m\dot{V}_a = T - D - W\sin(\gamma) \tag{A.1}$$

Then, the steady-state assumption, which sets $V_a = 0$, allows for thrust to be isolated. As discussed in section 2.1, this will both over and under approximate thrust, with any discrepancies largely canceling each other out.

$$T = D + W\sin(\gamma) \tag{A.2}$$

Next, the concise version of the power equation is presented.

$$P = T\frac{V_a}{\eta} \tag{A.3}$$

Equation A.2 is then substituted into Equation A.3.

$$P_{req} = (D + W\sin(\gamma))\frac{V_a}{\eta} \tag{A.4}$$

Drag is defined as

$$D = \frac{1}{2}\rho V_a^2 S C_D. \tag{A.5}$$

The expression for drag is then substituted into Equation A.4.

$$P_{req} = \frac{V_a^3 \rho S C_D}{2\eta} + \frac{V_a W\sin(\gamma)}{\eta} \tag{A.6}$$

The next term to be expanded is the coefficient of drag, which is defined as

$$C_D = C_{D0} + K C_L^2. \tag{A.7}$$

The coefficient of drag and drag polar coefficient are both constants. Therefore, the next step is to solve for the coefficient of lift, which is defined as

$$C_L = \frac{2L}{V_a^2 \rho S}. \tag{A.8}$$

Now, to solve for lift, another of the key dynamics functions introduced in Section 2.2.2 is utilized. The forces acting upon an aircraft in a coordinated turn are given by

$$L\cos(\phi) = W\cos(\gamma)/ \tag{A.9}$$

Next, the lift is isolated.

$$L = W\frac{\cos(\gamma)}{\cos(\phi)} \tag{A.10}$$

Equation A.10 is then substituted into Equation A.8.

$$C_L = \frac{2W}{V_a^2 \rho S}\frac{\cos(\gamma)}{\cos(\phi)} \tag{A.11}$$

Equation A.11 itself is then substituted into Equation A.11.

$$C_D = C_{D0} + K\left(\frac{2W}{\rho V_a^2 S}\frac{\cos(\gamma)}{\cos(\phi)}\right)^2 \tag{A.12}$$

With the coefficient of drag derived in Equation A.12, it is substituted into Equation A.6, to finally complete the expression for power required.

$$P_r = \frac{V_a^3 \rho S}{2\eta}\left(C_{D0} + K(\frac{2W}{\rho V_a^2 S}\frac{\cos(\gamma)}{\cos(\phi)})^2\right) + \frac{V_a W\sin(\gamma)}{\eta} \tag{A.13}$$

Then, the exponent is evaluated, terms are distributed, and like terms are simplified.

$$P_r = \frac{V_a^3 \rho S C_{D0}}{2\eta} + K\frac{2W^2}{\eta \rho V_a S}\frac{\cos^2(\gamma)}{\cos^2(\phi)} + \frac{V_a W\sin(\gamma)}{\eta} \tag{A.14}$$

Finally, common constants a defined as K_{p1} and K_{p2} in order to make their use in other equations more streamlined. This completes the derivation for power required — the cost

function for the trajectory optimization problem.

$$P_r = V_a^3 \rho K_{p1} + \frac{W^2}{V_a \rho} \frac{\cos^2(\gamma)}{\cos^2(\phi)} K_{p2} + \frac{V_a W \sin(\gamma)}{\eta} \tag{A.15}$$

where

$$K_{p1} = \frac{S C_{Do}}{2\eta} \qquad K_{p2} = \frac{2K}{\eta S} \tag{A.16}$$

A.2 Deriving Velocity for Minimum Power from the Cost Function

This section demonstrates that the velocity for minimum power can be derived power required established in Section 2.1.

$$P_r = V_a^3 \rho K_{p1} + \frac{W^2}{V_a \rho} \frac{\cos^2(\gamma)}{\cos^2(\phi)} K_{p2} + \frac{V_a W \sin(\gamma)}{\eta} \tag{A.17}$$

First, assuming level flight eliminates many terms.

$$P_r = V_a^3 \rho K_{p1} + \frac{W^2}{V_a \rho} K_{p2} \tag{A.18}$$

Then, set the derivative equal to zero to find the minimum.

$$\frac{\partial P_r}{\partial V_a} = 3 V_a^2 \rho K_{p1} - \frac{W^2}{V_a^2 \rho} K_{p2} = 0 \tag{A.19}$$

By multiplying by V_a^2 and then using the quadratic formula, the equation is put in terms of V_a^2.

$$V_a^4 (3 \rho K_{p1}) - \frac{W^2}{\rho} K_{p2} = 0 \tag{A.20}$$

$$V_a^2 = \frac{\sqrt{12 W^2 K_{p1} K_{p2}}}{6 \rho K_{p1}} \tag{A.21}$$

Next, terms are moved into the radical and both constants are replaced with how they were defined.

$$V_a^2 = \frac{2W}{\rho}\sqrt{\frac{K_{p1}K_{p2}}{12K_{p1}}} \tag{A.22}$$

$$V_a^2 = \frac{2W}{\rho}\sqrt{\frac{4K\eta}{12S^2\eta C_{D0}}} \tag{A.23}$$

And finally, simplifying like terms results in the airspeed for minimum power.

$$V_a^2 = \frac{2W}{\rho S}\sqrt{\frac{K_p}{3C_{D0}}} \tag{A.24}$$

A.3 Minimum Energy — Ordnance Drop

By utilizing the refined problem formulation from Section 4.5.2, without many changes, a time-on-target ordnance drop can be easily modeled. This can be accomplished by running 2 instances of the solver in series, needing only to modify the boundary conditions. Assume that the aircraft begins at a specified initial position, must arrive at a specified target, and then return to the initial position. First, define the time array with a set initial condition t_0, set time-on-target t_s, and unrestrained final time t_f. Then, update the first stage boundary conditions.

$$\Delta m(t_0) = 0 \qquad \Delta m(t_s) = 0 \geq \Delta m_s \geq \Delta m_e \tag{A.25}$$

$$x(t_0) = x_0 \qquad x(t_s) = x_s \tag{A.26}$$

$$y(t_0) = y_0 \qquad y(t_s) = y_s \tag{A.27}$$

$$z(t_0) = z_0 \qquad z(t_s) = z_s \tag{A.28}$$

$$t(t_0) = 0 \qquad t(t_s) = t_s \tag{A.29}$$

Then, for stage two, the initial conditions become the final conditions of stage one. And since it was specified to return to the initial position, those become the final conditions of

stage two.

$$\Delta m(t_s) = \Delta m_s \qquad \Delta m(t_f) = \Delta m_s \geq \Delta m_f \geq \Delta m_e \tag{A.30}$$

$$x(t_s) = x_s \qquad x(t_f) = x_0 \tag{A.31}$$

$$y(t_s) = y_s \qquad y(t_f) = y_0 \tag{A.32}$$

$$z(t_s) = z_s \qquad z(t_f) = z_0 \tag{A.33}$$

$$t(t_s) = t_s \tag{A.34}$$

A.4 GitHub Code Repository

The code used to initialize and execute DIDO [12], plot results, and all supporting functions can be found in the following GitHub repository:

https://github.com/llalumandier/Lalumandier_MSAE_Thesis.git

DIDO is a licensed product of Elissar Global. A MATLAB environment with DIDO [12] installed with an active license is required to execute this thesis' code.

A.5 Flypath3d Still Images

The aerospace visualization toolbox Flypath3d [17] was used to create animations of the trajectories of each of the results. In the text, the quiver plots of the trajectories are able to convey more information concisely, so these plots were omitted from the main body. However, for presentations animations are always a welcome addition. As such, still images of these animations have been included in this Appendix.

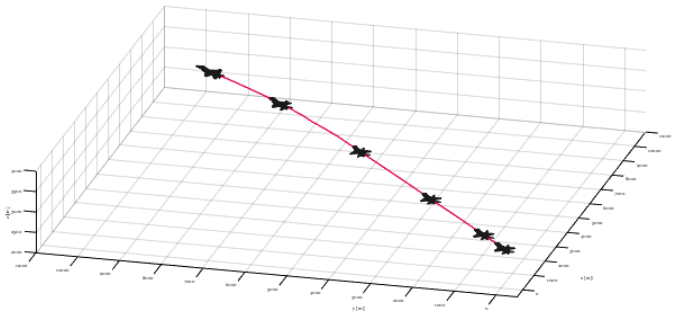

Figure A.1. Chapter 4 Trajectory

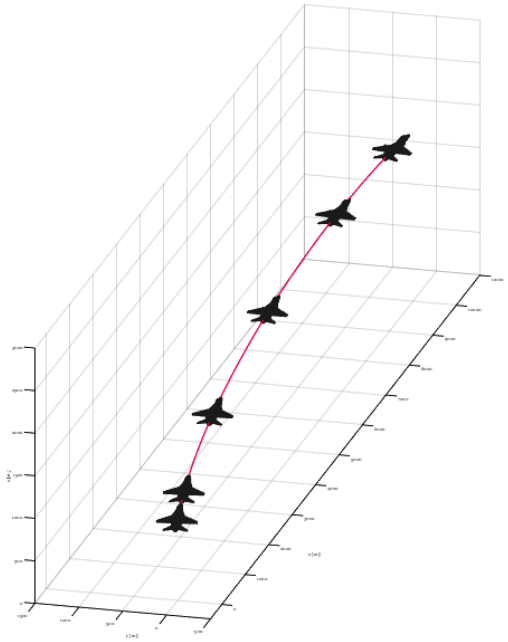

Figure A.2. Updraft Trajectory

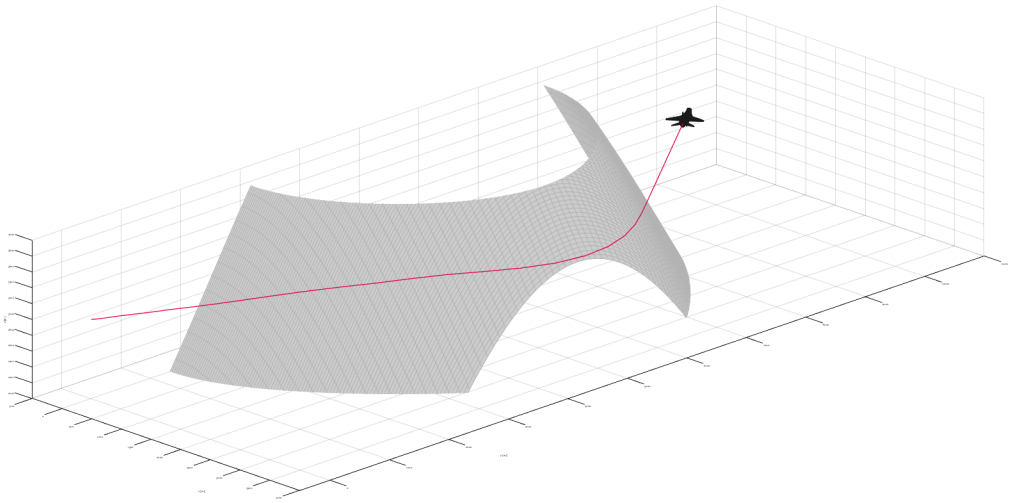

Figure A.3. Terrain Avoidance Trajectory

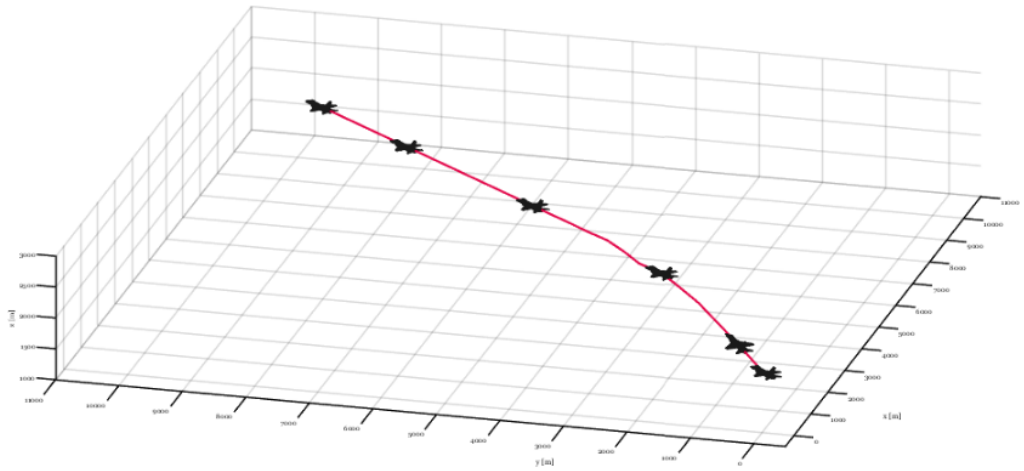

Figure A.4. Time-Varying Wind Trajectory

THIS PAGE INTENTIONALLY LEFT BLANK

List of References

[1] E. Zermelo, "Über das navigationsproblem bei ruhender oder veränderlicher windverteilung," *Zeitschrift für Angewandte Mathematik und Mechanik*, vol. 11, no. 2, pp. 114–124, 1931.

[2] R. Stroman and D. Edawrds, "The hybrid tiger: A long endurance solar/fuel cell/soaring unmanned aerial vehicle," US Naval Research Laboratory via Department of Energy, Jun. 14, 2018 [Online]. Available: https://www.hydrogen.energy.gov/pdfs/review18/ia005_stroman_2018_o.pdf

[3] M. Schutt, "Unmanned systems integrated battle problem 21 [image 1 of 3]," Defense Visual Information Distribution Service, Apr. 24, 2021 [Online]. Available: https://www.dvidshub.net/image/6615142/unmanned-systems-integrated-battle-problem-21

[4] Platform Aerospace, "Vanilla Smashes World Record:
> 8 days, >12,000 miles, Comms Package," Oct. 2021,
https://static1.squarespace.com/static/5b89a45fa9e02897af6fe886/t/6158e4950feb2e263fe0dd98/1633215637790/%28Oct+2021%29+Vanilla+Breaks+World+Record.pdf.

[5] S. Lee, "Energy optimal trajectory planning of long-endurance uav in time-varying energy fields," M.S. thesis, Dept. of Mechanical and Aerospace Engineering, NPS, Monterey, CA, USA, 2021 [Online]. Available: http://hdl.handle.net/10945/67759

[6] Vanilla Unmanned Aerial Systems, "Why Vanilla," Online, accessed: May 2023. Available: https://vanillaunmanned.com/why-vanilla

[7] Vanilla Unmanned Aerial Systems, "Vanilla UAS - Datasheet," Online, November 2022, accessed: May 2023. Available: https://static1.squarespace.com/static/5b89a45fa9e02897af6fe886/t/640b4b5b2cfc1942de846c64/1678461788143/%28Nov+2022%29+Vanilla+UAS+-+Multi-Domain+Datasheet.pdf

[8] MIT Department of Mechanical Engineering, "Specific heats of gases," https://web.mit.edu/16.unified/www/FALL/thermodynamics/notes/node97.html, n.d.

[9] "U.S. Standard Atmosphere, 1976," National Oceanic and Atmospheric Administration, 1976. Available: https://ntrs.nasa.gov/api/citations/19770009539/downloads/19770009539.pdf

[10] R. M. Hodur, "The coupled ocean/atmosphere mesoscale prediction system (coamps)," *Monthly Weather Review*, vol. 125, no. 7, pp. 1414–1430, 1997.

[11] National Oceanic and Atmospheric Administration, "HRRR model information," https://rapidrefresh.noaa.gov/hrrr/, Accessed 2023.

[12] I. M. Ross, *A Primer on Pontryagin's Principle in Optimal Control*, second edition ed. San Francisco: Collegiate Publishers, 2015.

[13] I. M. Ross and Q. Gong, "Guess-free trajectory optimization," AIAA/AAS Astrodynamics Specialist Conference and Exhibit, Honolulu, HI, 2008.

[14] I. M. Ross, Q. Gong, M. Karpenko, and R. J. Proulx, "Scaling and balancing for high-performance computation of optimal controls," *Journal of Guidance, Control, and Dynamics*, vol. 41, no. 10, pp. 2086–2097, oct 2018. Available: https://doi.org/10.2514%2F1.g003382

[15] T. G. Farr, P. A. Rosen, E. Caro, R. Crippen, R. Duren, S. Hensley, M. Kobrick, M. Paller, E. Rodriguez, L. Roth, D. Seal, S. Shaffer, J. Shimada, J. Umland, M. Werner, M. Oskin, D. Burbank, and D. Alsdorf, "The shuttle radar topography mission," *Rev. Geophys.*, vol. 45, pp. –, may 2007. Available: http://dx.doi.org/10.1029/2005RG000183

[16] V. Dobrokhodov and K. Jones, "Energy-aware autonomy of group 2 uas utilizing environmental energy sources," NPS Department of Mechanical and Aerospace Engineering Research Portfolio, 2021.

[17] W. Bużantowicz, "Matlab script for 3d visualization of missile and air target trajectories," *International Journal of Computer and Information Technology*, vol. 05, no. 05, pp. 419–442, 2016.

Initial Distribution List

1. Defense Technical Information Center
   Ft. Belvoir, Virginia

2. Dudley Knox Library
   Naval Postgraduate School
   Monterey, California